Department of Physics and Astronomy
University of Heidelberg

Bachelor Thesis in Physics
submitted by

Niklas Wahl

born in Heidelberg (Germany)

2011

Performance of the local on-line Tracking and of a track-based Jet Trigger Algorithm for the ALICE TRD on the Basis of Monte-Carlo Simulations

This Bachelor Thesis has been carried out by Niklas Wahl at the
Physikalisches Institut in Heidelberg
under the supervision of
Prof. Dr. Johanna Stachel

Abstract (English): The high interaction rates at modern particle colliders like the LHC require triggers to identify signatures of rare interactions and select these events during the data taking. With the TRD at ALICE a track-based jet trigger shall be realised which detects showers of high-momentum particles within approximately $7\,\mu$s to contribute to the L1 trigger. The performance of such a jet trigger will be studied in the first part of this thesis for the idealistic case on Monte-Carlo level by analysing the efficiency for selecting jet events and the rejection of minimum bias events. As the performance of the trigger especially depends on the precise determination of the tracklets in the individual chambers of the TRD, the second part of this thesis adresses the analysis of the local tracking by the multi-chip modules on the TRD chambers. There the focus lies on the effects of the ALICE solenoid field and a tail cancellation filter with respect to efficiency, noise and resolution of the tracklets and their dependency of the directly within the electronics configurable parameters.

Abstract (German): Die sehr hohen Wechselwirkungsraten bei modernen Teilchenbeschleunigern wie dem LHC verlangen Trigger, die Signaturen seltener und interessanter Wechselwirkungen erkennen und diese Ereignise noch während der Datennahme auswählen. Mit dem TRD des ALICE-Experiments soll ein spurbasierter Jet-Trigger realisiert werden, der innerhalb von ca. $7\,\mu$s Schauer von Teilchen mit hohem Impuls entdeckt und so ein Signal zum L1 Trigger beisteuern kann. Die Leistungsfähigkeit eines solchen Jet-Triggers wird im ersten Teil dieser Arbeit für den Idealfall auf Monte-Carlo Ebene untersucht, indem die Effizienz der Auswahl von Jet-Ereignissen und die Ablehnung von minimum-bias Ereignissen analysiert wird. Da die Leistungsfähigkeit des Triggers vor allem von der präzisen Bestimmung der Spurabschnitte in den einzelnen Kammern des TRD abhängt, widmet sich der zweite und größere Teil der Arbeit der Analyse der lokalen Spurrekonstruktion in den Multi-Chip-Modulen auf den TRD Kammern. Dabei wird vor allem die Wirkung des ALICE-Magnetfeldes sowie eines Filters zur Ionenschweifunterdrückung auf Effizienz, Rauschen und Auflösung der Spurabschnitte und deren Abhängigkeit der direkt in der Elektronik konfigurierbaren Parameter untersucht.

Contents

1 Introduction

1.1 Motivation

Almost one percent of the world's information production rate arises from the detectors at the **L**arge **H**adron **C**ollider (LHC) at the European Organization for Nuclear Research (CERN)[CER06] when either protons or lead-ions are smashed into each other several million times a second, leaving physicists with petabytes of data and the will to round out our theories and to reveal more about the first split seconds of our universe. The observation of those collision events rise to a vehement challenge. Since the interaction itself cannot be studied directly, the only chance lies in chasing down all the particles flying away from the collision and translating their special signature of their origin and interactions, respectively their momentum, charge, mass etc. into results that allow a conclusion on the processes nobody can see directly. Therefore huge and complicated detector systems are needed, to track down every interesting signal and allow precise measurements of the tracks the particles travel within the detectors. Furthermore, if one considers the small cross sections the most interesting processes hold, a detailed analysis seems like looking for a needle in the haystack. As a consequence it is desirable to find evidences for signatures like particle jets, angular distribution of specific particles or the like for important decays and interactions already online[1] and discard the more ordinary events from being recorded or even read out (so called "triggering"). Highly complex detectors are necessary to meet those requirements. One of them is the transition radiation detector of **A** **L**arge **I**on **C**ollider **E**xperiment (ALICE) at the LHC, which will be discussed in this thesis with a focus on the accurate determination of track segments of high momentum particles.

With the assistance of all the other detectors in ALICE one fondly hope to get a better understanding of the Quark-Gluon-Plasma (QGP) [ALI10], a state of very hot and dense matter expected to have been existing shortly after the big bang, where quarks and gluons are not longer "glued" together due to the confinement of the strong force [ALI07]. This state can be achieved shortly after the collision of lead ions, and the information of the particles interacting with the QGP will hopefully provide us more insight to its characteristics.

---

[1] "Online" involves all the processes that run during the raw data acqusition while "offline" implies all the computing (including reconstruction and analysis) that is done afterwards.

After this introduction a short summary of the theoretical background and physical motivation is given. From section 2.1 to 3, the setup of the LHC is outlined with focus on the ALICE detector and espically it's transition radiation detector. 3 also includes a study about triggering on jet events. Then, in section 4 the particle detection and tracking procedure of this detector will be explained to prepare for 6, in which the results of the analysis will be presented.

1.2 The Standard Model of Particle Physics

The searches for smaller and smaller elementary particles, beginning with the discovery of the atom in the early beginning of the 20th century, have led to a gauge theory for 12 particles, the so called fermions, interacting through three fundamental forces called the strong force, the weak force and the electromagnetic force. The fourth fundamental force, the gravitation, is still withstanding all attempts of a quantisation which fits into the quantum field theories of the Standard Model, therefore it is not included [Ber06]. As figure 1.1 shows, the 12 particles can be devided into quarks and leptons and furthermore into three families, also called generations. Almost all "common" matter is built out of the first generation's particles, as they are the only stable ones. With increasing generation number, the particles become heavier and their lifetime decreases.

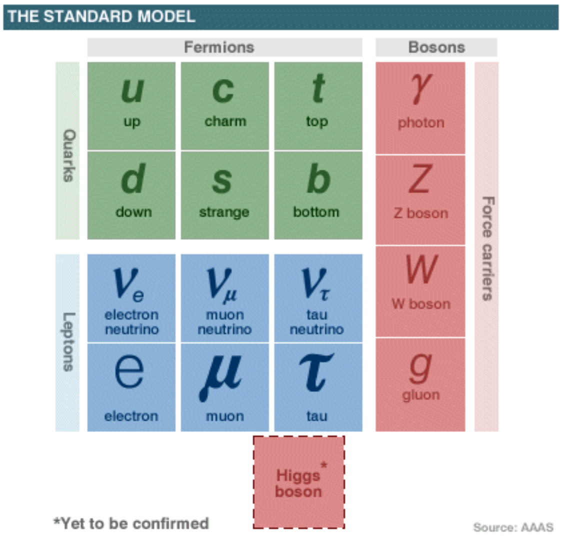

Figure 1.1: The Standard Model of particle physics: The fermions (quarks and leptons) are split up in three so called generations (columns). The four bosons deliver the strong (g), weak (Z,W) and electromagnetic force (γ). The higgs boson is supposed to give the elementary particles their mass, but could not be found yet.

In aiddtition, four gauge bosons exist to deliverer the fundamental forces. The gluon is responsible for the strong interaction between the quarks, the W and Z boson deliver the weak force and the photon the electromagnetic force between quarks and leptons.

The famous Higgs boson, which's existence could not be confirmed yet, is believed to give the particles their mass by delivering the interaction between them and the Higgs field.

1.3 Jets

Jets belong to the most interesting phenomena in high energy particle collisions. They owe the confinement for strong interacting particles their existence: Initial hard scattering partons, diverging from each other, will gain more and more energy. This leads to radiation of gluons, the pair-production of new partons and anti-partons immediately forming hadrons. The resulting cascade of these hadrons is called jet (figure 1.2).

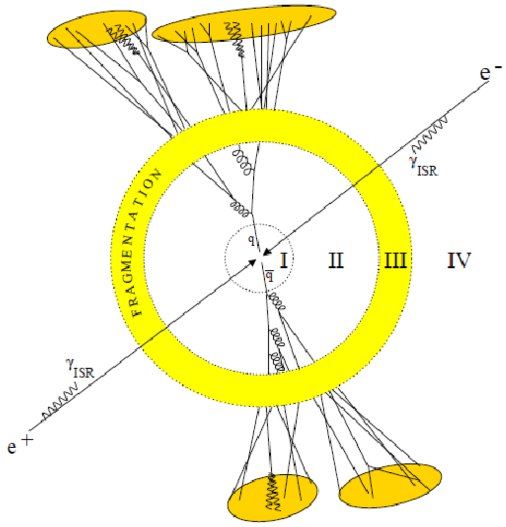

Figure 1.2: Schematic view of the jet formation by the example process $e^+e^- \rightarrow Z_0/\gamma \rightarrow q\bar{q}/gq\bar{q}g$. The hard scattering occurs in phase **I**, followed by hard and soft gluon radiation in phase **II**. The initial partons and hard scattered gluons fragment to hadrons in phase **III** to the jets. In Phase **IV** the remaining instable particles decay into stable ones. [Fla01]

In high energy particle collisions like the ones performed at the Large Hadron Collider (LHC) or also the former Large Electron Positron Collider (LEP) at CERN, the momentum of the hard scattered particles is high enough for a possible hard radiation of gluons. As the propability of gluon radiation depends on α_s and the corresponding colour factor [Fla01], one can translate this into a proprtionality for the number of jets found in the events and also the angular distributions, according to the physical processes one wants to observe.

The analysis of jet energy, number of jets and angular distributions makes it possible to look deep into the fundamental processes of the strong interaction, and has e.g. lead to the discovery of the gluon [B$^+$79] and can also state as a proof for the gluon self coupling and finally a confirmation of the QCD as a SU(3) gauge-group [Col03].

By colliding hadrons instead of leptons (LHC ↔ LEP) the situation becomes more complicated, but also more interesting:

Proton-proton collisions

In *pp*-collisions, jets can not only be caused by hard processes between the valence and sea quarks within the protons (so called “final state” radiation) but also by gluon radiation shortly before the collision (“initial state” radiation) [EHH$^+$07].

With the high energy of the *pp*-collisions at the LHC, one goal is to find evidence for the existence of the Higgs boson or at least recieve further restrictions for its possible mass. The Higgs boson itself is believed to decay into W, Z or γ bosons. As these bosons themselves decay into quarks and leptons, he analysis of jets is an important chapter in the search for the higgs besides the investigation of the decays into leptons.

Heavy Ion collisions

In heavy ion collisions (in the LHC case lead-lead) one gets strong deviations from the jet spectra found in proton-proton collisions, as the case is even more complicated. In *pp*, the partons find themselves in free space after the scattering, while in collisions of whole atomic nuclei they have to deal with the hot and dense matter shortly after the collision of the both atomic nuclei. The interaction with this Quark-Gluon-Plasma (QGP), where due to the high energy quarks and gluons can exist in a free state, leads to a drastic energy loss of the partons, resulting in jets with much lower energy than in *pp*-collisions. This process called *Jet Quenching*, leads to a symmetry breaking in the energy of initially back to back emitted jets. Thus, by observing the jet spectra of heavy ion collisions, conclusions about the structure and behaviour of the GQP can be drawed.

2 The Experiment

2.1 The Large Hadron Collider

After the Large Electron Positron Collider (LEP) at the European Center for Nuclear Research (CERN) served high energy physics well for over 10 years and finally reached its energetic limits at 209 GeV, the way was cleared for the construction of a hadronic collider with an energy range of several TeV. Using the already existing tunnel with an circumference of nearly 27 km, this project has been realised as zhe **L**arge **H**adron **C**ollider (LHC) which finally started operation in August 2009[1]. At the moment it is the most powerful hadronic accelerator ever built, with an energy of 3.5 TeV per beam resulting in center of mass energy of $\sqrt{s_{pp}} = 7\,\mathrm{TeV}$ for *pp*-collisions and an energy of 2.76 TeV per nucleon pair, resulting in a maximum obtainable center off mass energy of $\sqrt{s_{PbPb}} \approx 1150\,\mathrm{TeV}$. The energy for *pp*-collisions will even be raised to 7 TeV per beam and thus to $\sqrt{s_{pp}} = 14\,\mathrm{TeV}$ [Gro08].

For the hadrons the road to almost lightspeed is a long one, shown in figure 2.1. The injection into the LHC's main ring happens at 450 GeV for protons and 177 GeV/u for lead ions. Beforehand, the hadrons pass through linear accelerators and storage rings to gain the necessary momentum stepwise. In the very first step the protons are extracted by stripping away the electrons of hydrogen atoms, while for the lead ions this needs to be done within three steps during the pre-acceleration, finally gaining fully stripped Pb^{82+} ions [Wal10].

The major experiments of the LHC are installed at the four collision points of the opposed flying beams, while some addtitional smaller ones are set up between them. Two of the main experiments, **A T**orodial **L**HC **A**pparatus (ATLAS) and **C**ompact **M**uon **S**olenoid (CMS), inter alia serve the anticipated discovery of the Higgs-Boson by detecting a very broad range of particles, following different technological approaches. Simply put, ATLAS relies mainly on transition radiation tracking, calorimetry and muon detection, while CMS is, as its name says, focused on muon detection with a very high solenoid field of 4 T flowing through mainly silicon detectors and electronic/hadronic calorimetres [CER11].

---

[1] Technical problems which damaged the beam pipe among others shortly after the original start in 2008 led to a delay of 11 months

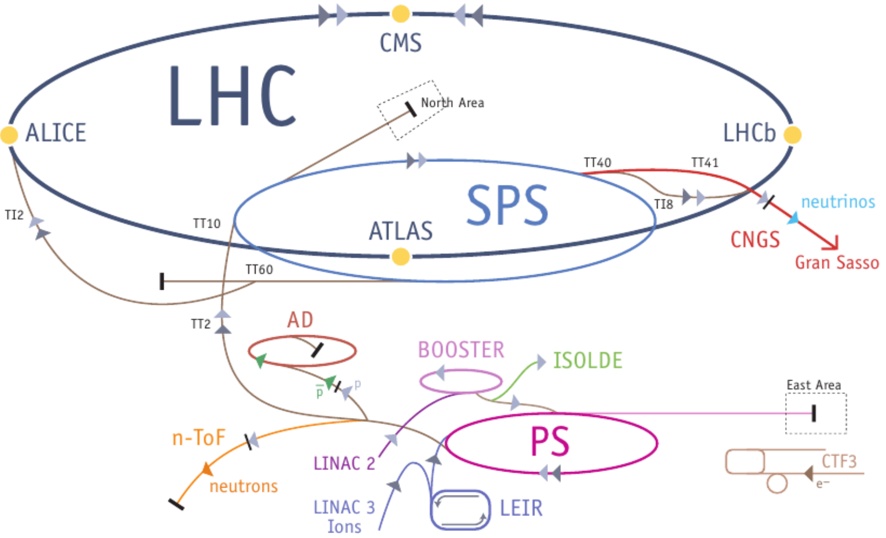

Figure 2.1: Overview of the LHC with the pre-accelerator chain. Protons travel from their stripping point to the linear accelerator LINAC 2 to be then further boosted by BOOSTER, the Proton Synchrotron (PS) and finally the Super Proton Synchrotron (SPS) before injected into the main ring. Lead ions travel via the LINAC 3 and the Low Energy Ion Ring (LEIR) to the PS, being stripped two times before LEIR and one time before SPS.[Gro08]

To analyse the decay physics of hadrons containing bottom (also called beauty) quarks, the B-mesons, the **L**arge **H**adron **C**ollider **b**eauty (LHCb) was designed as a forward spectrometer, considering the relatively small emission angle of B-mesons with respect to the beam axis. It uses **R**ing **I**maging **C**herenkov detectors (RICH) for particle identification, silicon detectors for tracking and hadronic and electromagnetic calorimeters for energy measurements. Also several muon spectrometers are present, and a vertex locator to determine the secondary B-decay vertices as precisely as possible. By a detailed analysis of the B-meson decay with respect to CP-violation, one hopes to get a better understanding of the unbalanced existence of matter and antimatter in our universe.

The last but not least of the four experiments is **A** **L**arge **I**on **C**ollider **E**xperiment (ALICE) designed to observe and analyse the collisions of the lead ions with the intention to get more information about the structure and the existence of the QGP, the state of matter shortly after the big bang, which can be produced by central collisions of two lead ions. The structure and design considerations are explained more detailed in section 2.2.

In addition three smaller experiments have been installed at LHC. TOTEM (**Tot**al **E**lastic and diffractive cross section **M**easurement) determines the cross section of central pp-collisions and the LHC's luminosity. Measurements the luminosity and data collection for the calibration of other detectors be done with **LHC** **f**orward (LHCf), a small detector setup near ATLAS, while the last installed **Mo**nopole and **E**xotics **D**etector **A**t the **L**HC (MoEDAL) looks for magnetic monopoles and exotic, eg. supersymmetric, particles.

2.2 The ALICE Experiment

ALICE is one of the four big experiments at LHC and especially designed for taking data from heavy ion collisions, in the LHC case lead-lead events at a maximum center of mass energy of $\sqrt{s} = 2 \cdot 2.76\,\mathrm{GeV}$ per nucleon pair. It has an overall size of $26 \times 16 \times 16\,\mathrm{m}^3$ and weighs about 10000 t[A$^+$08a]. The experiment consists of the central barrel part around the interaction point for the tracking and identification of photons, electrons and hadrons and a forward muon spectrometer. The set up is shown in figure 2.2.

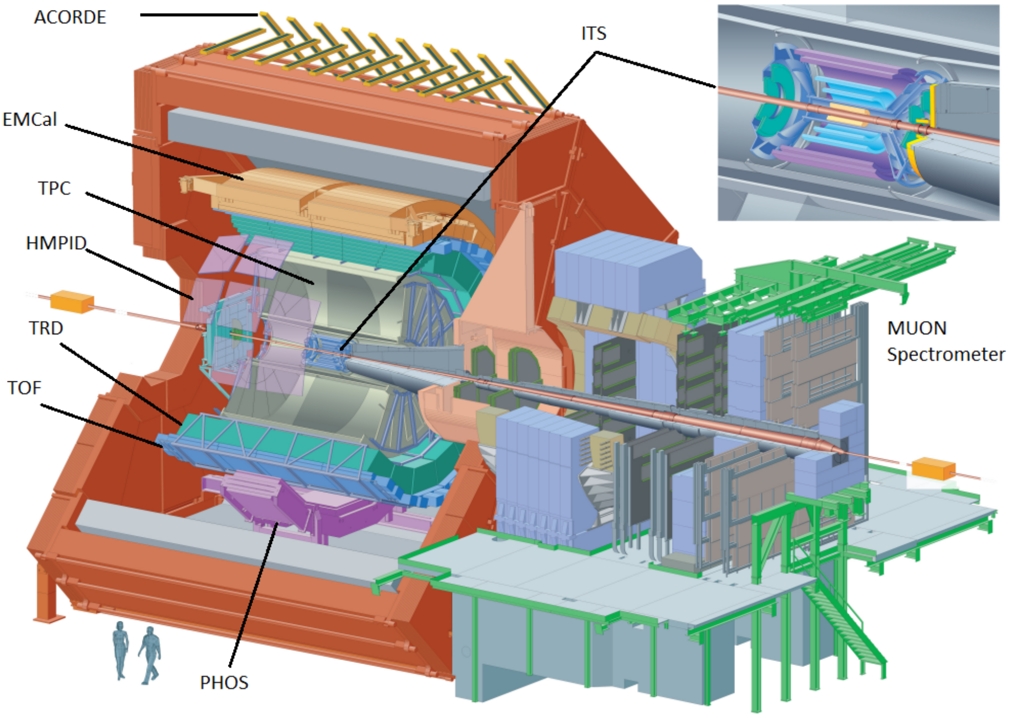

Figure 2.2: Schematic layout of the ALICE detector. On the left side one can see the central barrel while on the right side the muon spectrometer is shown. The box on the upper right shows a closer view of the detector components close to the interaction point. [A$^+$08a]

Most of the detectors were designed to work at charged particle multiplicities of $\mathrm{dN_{ch}/d_\eta} = 8000$ whereby the last measured value is $\mathrm{dN_{ch}/d_\eta} = 1584 \pm 4(\mathrm{stat}) \pm 76(\mathrm{syst})$ [A$^+$10]. In comparision to the other experiments, ALICE is also optimized to detect low momentum particles as shown in figure 2.3 due to the low momentum dominated spectra in heavy ion collisions.

2.2.1 Central Barrel Detectors

Starting at the interaction point (IP) and going out in radial direction, the central barrel consists of the **I**nner **T**racking **S**ystem (ITS), a **T**ime **P**rojection **C**hamber (TPC), the **T**ransition **R**adiation **D**etector (TRD) followed by a **T**ime **O**f **F**light (TOF) and the **H**igh

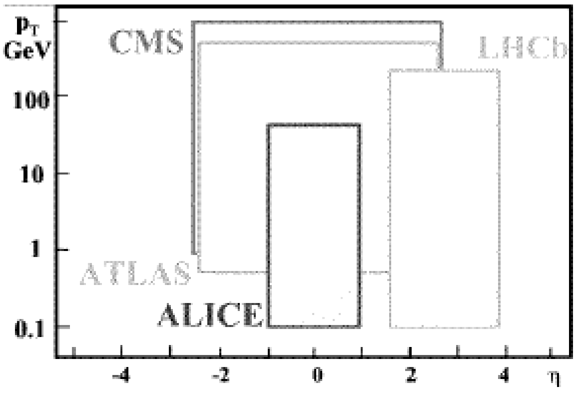

Figure 2.3: Comparison of the p_T and η coverage of the central barrel detectors of the LHC [Sch08].

Momentum **P**article **ID**entification (HMPID) detector . These are the main detectors for tracking and particle identification (PID) covering (expect for the HMPID) the whole azimuth and an η-range (pseudo-rapidity) of at least ± 0.9.

The outer detectors are a **Ph**oton **S**pectrometer (PHOS) and an **E**lectro**m**agnetic **Cal**orimeter (EMCal). The detectors are surrounded by a solenoid magnet which creates a homogenous field in the beam direction of about 0.5 T. The field leads to a curvature of the charged particles depending on the transverse momentum p_T and hence allows a precise momentum measurement.

In more detail, the ITS contains three sub-detectors with each two layers. It's main purpose is to determine the primary vertex and distinguish it from the secondary decay-vertices. Also, it shall provide tracking and particle identification for low momentum particles (below 200 MeV/c). The first sub detector is a two-layer **S**ilicon **P**ixel **D**etector (SPD) followed by a **S**ilicon **D**rift **D**etector (SPD) for the next two layers and finally another two layers of a **S**ilicon micro-**S**trip **D**etector (SSD). The ITS approximately covers radii from 4 cm to 43 cm and an η-range of ± 0.9 for the four outer layers, while the innermost layers cover up to ± 2 in η.

The TPC, located between[2] $r = 61\,\text{cm}$ and $r = 278\,\text{cm}$, is the main tracking detector within the central barrel and participates on PID by an accurate energy loss measurement and the determination of the vertex position, whereby it's main disadvantage is a slow working rate due to the long drift time in comparision to the other detectors.. However, the TPC is able to cover a large p_T-range from 100 MeV/c up to 100 GeV/c with good momentum resolution. It has a cylindrical shape and is filled with $90\,\text{m}^3$ gas being ionized by traversing charged particles. The usual η-coverage, given by the geometry of the TPC, lies within ± 0.9, while it is possible to widen it up to $|\eta| = 1.5$ if one doe can live with the reduced tracklength and the worse momentum resolution. The TPC also covers the whole azimuth.

---

[2] outer dimensions; the actually active volume is $85\,\text{cm} < \text{r} < 247\,\text{cm}$

As its name implies the TRD uses "Transition Radiation" (TR) (section 3.1.1) to identify electrons and reject pions above a momentum of 1 GeV/c. It is also capable of a fast determinition of the track p_T and thus a very important tracking detector and can also be used as a trigger for charged particles with high momentum, to select for example jet events or reject events with low multiplicity. Also the specific energy deposit of electrons due to TR makes it possible to realise an e^+e^--trigger to achieve better signal-to-noise ratios, e.g. for Υ-decays. It is arranged in 18 supermodules[3] in ϕ-direction (each covering about 20°) containing 5 modules in η, each covering a pseudo-rapidity range of approximately 0.36. Every module has 6 layers in the radial direction and lies within $2.90\,\mathrm{m} < \mathrm{r} < 3.68\,\mathrm{m}$. The TRD is outlined in figure 2.4 and will be explained more detailed in section 3 since the studies of this thesis focus on it.

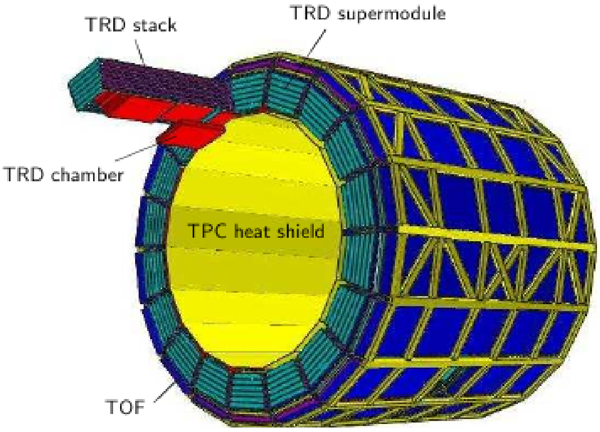

Figure 2.4: Drawing of the TRD in the space frame with the attached TOF-detector.[A$^+$08a]

Closely to the TRD at $r = 3.7\,\mathrm{m}$ and with a radial thickness of approximately 30 cm the **T**ime **Of** **F**light (TOF) detector is located to strongly contribute on PID for pions, kaons and protons in the medium momentum range (up to 2.5 GeV/c for Kaons/Pions and 4 GeV/c for protons). As the TRD, it is split up in 18 supermodules in ϕ each containing 5 modules in η. It is able to measure the flight time of a particle from the vertex to the detector with a time resolition of better than 40 ps and an efficency of almost 100% due to the use MRPC (**M**ulti-gap **R**esistive-**P**late **C**hambers).

In addition, to identify higher momentum particles beyond the limits of TOF, ITS and TPC the HMPID is used. It only covers an η-range of ± 0.6 and 57.6° in ϕ and is located at a radial position of 5 m. Also only partially covering the azimuth from 220° to 320°, the PHOS lies at $r = 4.6\,\mathrm{m}$ and whithin $\eta = \pm 0.12$. It's main purposes are measurements of low p_T photons and correlations between high-p_T π^0 and photons to study the initial phase of the collision and jet-quenching. The last important remaining detector of the central barrel is the EMCal, located in the opposite direction of the PHOS. It's main

---

[3] At the moment (April 2011) not all supermodules are installed

task is the exploration of jet physics, as it is able to determine the neutral energy deposit of jets and thus giving a good jet energy resolution not only for *pp* but also for *PbPb* collisions. With the EMCal, one can distinguish jets from the large background and is able to detect important effects of jet-quenching. It covers, like the PHOS, 107° in ϕ but a larger pseudo-rapidity range of ± 0.7 and lies at a radius of 4.5 m.

Last but not least, at the outside of the central barrel on top of the solenoid coil the **A**LICE **C**osmic **R**ay **De**tector (ACORDE) is located to contribute on the L0-trigger (section 2.2.3) for some detectors and to detect muon events together with the TPC and TRD to study cosmic rays.

2.2.2 Forward Detectors

The biggest forward detector is the muon spectrometer (MUON) which is located next to the central barrel and covers an η-range of -4.0 to -2.5 and the whole azimuth to measure the $\mu^+\mu^-$ decay channel for heavy quark vector mesons like the J/Ψ and the Υ and provides an opportunity to examine the production of open heavy flavours.

To determine the centrality and multiplicity of mainly the PbPb collisions and to function inter alia as a L0 trigger, some smaller detectors are installed. The **Z**eroe **D**egree **C**alorimeter (ZDC) is installed symmetrically on both sides of the IP and is split up in two detectors for neutrons (ZN) and protons (ZP) on each side at 115 m and two electromagnetic calorimeters (ZEM) next to the beam pipes 7 m away from the interaction point. They measure the number of so called spectator nucleons to determine the number of participating nucleons[4] in the collision which directly allows a conclusion for the centrality of the detected event. The ZDC is supported by the **F**orward **M**ultiplicity **D**etector (FMD) to measure the multiplicity of charged particles and directly connects to (and partially overlaps with) the pseudo-rapidity range of the ITS (together they cover a range from $-3.4 < \eta < 5.0$). One of the tasks of the T0 and V0 detectors is to generate a very fast trigger signal for the central barrel detectors. V0 is installed on both sides of the interaction point, one at a distance of 90 cm and another at 360 cm on the other side to generate a minimum-bias trigger signal by counting charged particles from the collision by observing the beam gas rejection or also a signal for a multiplicity and centrality trigger. To get a very early signal which is needed to set a start time for the TOF and to wake up the TRD-electronics yet before the L0-trigger, two arrays of the T0 were installed at 72.7 cm on the one side and 375 cm on the other from the IP. It is also able to measure the primary vertex position with a resolution of ± 1.5 cm or, like the V0, generate minimum bias or multiplicity/centrality triggers.

---

[4] $N_{participants} = N_{Pb} - N_{spectators}$

2.2.3 ALICE Trigger System

Due to the high luminosity for pp-and the very high multiplicities in $PbPb$-collisions, it is necessary to select events of a common interest already online to reduce the bandwith and stored data. To fulfill this requirements, a multilevel trigger system is implemented in ALICE, divided into the pre-trigger (only for the TRD), the L0, L1, L2 triggers and the High-Level-Trigger.

The **pre-trigger** and the **L0**-trigger signals are mainly delivered by the forward detectors and by ITS, but partially also by the other central barrel detectors like for example the EMCal. While the L0-trigger has to be sent to the **C**entral **T**rigger **P**rocessor (CTP) within 800ns to be interpreted there and then forwarded after 1.2 μs to the central barrel detectors to activate them[5], the pre-trigger signal directly activates the TRD electronics ("wake up" trigger).

Till 6.2 μs after the L0 activation, the detectors not fast enough to contribute to L0 (or only just activated by L0) can contribute a signal to the **L1**-Trigger which completes the fast triggering. The L1 triggers on several event characteristics, like minimum bias, centrality, high p_T, assumed jets or also on certain particles and, if the event is accepted by L1, gives the detectors the green light for processing the final data and buffer it until the L2-accept.

The long latency of 100 μs till the **L2** trigger after the L0 is a consequence of the long drift time in the TPC. As the L1 trigger leads to a better and more precise calculation of the basic event information within the detectors, the L2 can use this information to give the final OK for the data transfer to the Data Aquisition System (DAQ) by passing the High-Level Trigger (HLT) The HLT performs a local and global reconstruction to subsequently compress the data and is so able to reduce the bandwith of max. 25 GB/s after the L2 to about 1 GB/s.

The Trigger system of the TRD will be explained in more detail in section 3.4.

---

[5] The detectors activated by L0 can vary based on the L0 inputs arriving at the CTP

3 The Transition Radiation Detector

Due to the high number of produced pions in lead-lead collisions, it is absolutely necessary to distinguish them from the rare and thus way more interesting electrons which don't obey the strong force and thus are very conducive to a detailed analysis of the interaction's initial processes. For low momenta, the dE/dx measurement of the TPC is satisfactory, but above 1 GeV/c the pion rejection is insufficient. The Transition Radiation Detector, already explained to some extent in section 2.2.1, especially provides this electron identification and pion rejection above 1 GeV/c and strongly contributes on the tracking of charged particles with 540 detector modules and an overall covered area of 694 m^2 [Col01]. Furthermore, it shall be used as a trigger on rare events.

3.1 Physics and Operation Principle

3.1.1 Transition Radiation

Transition radiation is caused by relativistic charged particles crossing the boundary between two media of different dielectric constants. It's dependency on the Lorentz factor γ in energy (eq. 3.1) and intensity makes it possible to distinguish light particles from heavier ones, as the case may be electrons from hadrons like pions by the choice of an appropriate radiation material.

Generally, the energy spectrum of transition radiation can be described by the following equation [Col01]:

$$\frac{\mathrm{d}^2\mathrm{W}}{\mathrm{d}\omega\mathrm{d}\Omega} = \frac{\alpha}{\pi^2}\left(\frac{\theta}{\gamma^{-2}+\theta^2+\xi_1^2} - \frac{\theta}{\gamma^{-2}+\theta^2+\xi_2^2}\right)^2 \quad . \tag{3.1}$$

The validity of this equation is limited to $\gamma \gg 1$, $\xi_i \ll 1$, $\theta \ll 1$, where $\gamma = \frac{E}{m_0c^2}$ is the Lorentz factor, $\xi_i = \frac{\omega_{P,i}^2}{\omega}$ with the material dependend plasma frequency $\omega_{P,i} = 28.8\sqrt{\rho\frac{Z_i}{A_i}}$ for the two media and $\alpha = 1/137$ the fine structure costant. ξ can also be written as $\xi_i = 1 - \epsilon_i(\omega)$ which illustrates the dependence on the dielectric constants of the two media.

The angular distribution θ has its maximum at $\theta = 1/\gamma$ and becomes highly collimated for increasing particle energies. This allows an integration over Ω which leads to the differential energy spectrum

$$\left(\frac{\mathrm{dW}}{\mathrm{d}\omega}\right) = \frac{\alpha}{\pi^2}\left[\frac{\xi_1^2+\xi_2^2+2\gamma^{-2}}{\xi_1^2-\xi_2^2}\ln\left(\frac{\gamma^{-2}+\xi_1^2}{\gamma^{-2}+\xi_2^2}\right)-2\right] \quad . \tag{3.2}$$

For large differences of the two plasma frequencies (e.g. $\hbar\omega_{P,air} = 0.7\,\mathrm{eV}$ and $\hbar\omega_{P,polyethylene} = 20\,\mathrm{eV}$) the energy can be approximated as [Boc98]

$$W \approx \frac{2}{3}\alpha\gamma\hbar\omega_{plasma} \tag{3.3}$$

where ω_{plasma} is the squared difference between the two plasma frequencies, wheras the average number of radiated photons is averaged by

$$\langle N\rangle \approx \alpha\gamma\frac{\hbar\omega_{plasma}}{\hbar\langle\omega\rangle} \quad . \tag{3.4}$$

Thanks to the comparatively very small mass of the elctrons in relation to hadrons like pions or protons, the Lorentz factor γ is much larger for them than for the heavier hadrons. Through the dependency of the average number $\langle N\rangle$ of radiated TR on γ, the choice of a suitable radiator forces only electrons to significantly radiate tranisition photons and hence leads to a comfortable way for their identification and rejection of other particles.

3.1.2 Particle Detection

To detect and identify charged particles crossing the TRD one uses **M**ulti-**W**ire **P**roportional **C**hambers (MWPC) with a drift chamber and the radiator installed in front (fig. 3.1). The particles crossing the radiator afterwards ionise the gas-mixture within the chamber, causing several electron clusters along the particles track starting to drift towards the MWPC pads. Due to the different starting point at the approximately same time, the original ionisation position can be obtained by evaluating the time-information of the charge deposition on the different cathode pads. If the particle emits a transition radiation photon this will ionise the gas close to the entrance of the chamber, causing a peak at later drift times in the pulse height spectrum (fig. 3.1). The first peak is the amplification peak which is caused by the ions out of the amplification region hitting the anode wires from both sides [Col01].

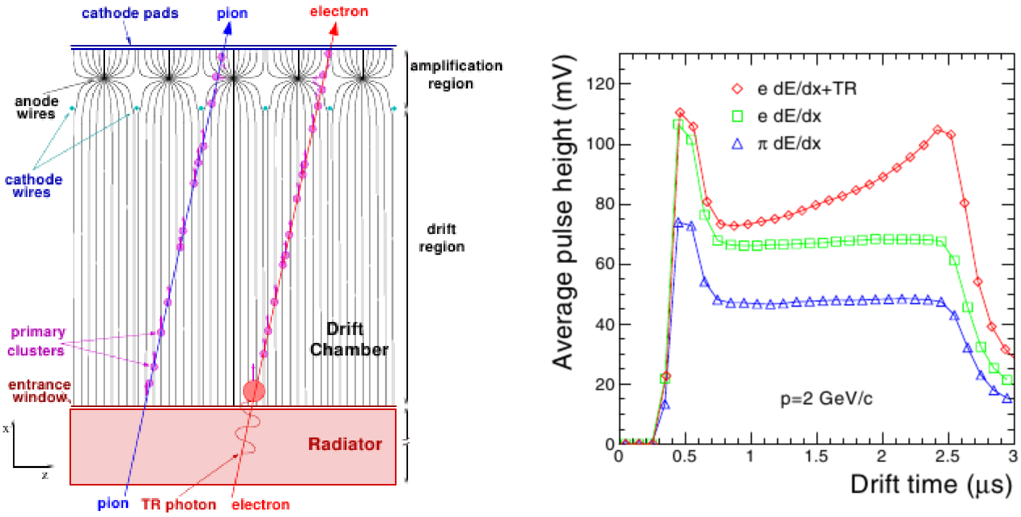

Figure 3.1: Left: View of an MWPC with a drift chamber. A crossing particle passes the radiatior to eventually cause TR and then ionizes the gas mixture within the chamber. Right: Calculated pulse height spectrum of pions, electrons and electrons caused a TR photon (resulting in an additional charge deposition). By evaluating the charge deposit it is possible to distinguish between electrons and pions. [A$^+$08a]

3.2 Structure

As already mentioned, the TRD is arranged in 18 supermodules around the beam axis, thus covering the whole azimuthal angle. Each supermodule consists of five stacks along the beam axis which an η coverage of about 0.36 each, leading to an total pseudo-rapidity range of $|\eta| = \pm 0.9$. To reduce the material budget in front of the PHOS, the three lower involved supermodules do not contain stack number 2. Each stack consists of 6 modules layered radially with several **R**ead-**O**ut **B**oards (ROB) containing the **M**ulti-**C**hip **M**odules (MCM) reading out the pad information. The close installation of the MCMs to the pad plane allows low signal loss and a fast evaluation of the pad information to provide the fast trigger signal.

In z-direction each detector module contains 16 pad rows (except for stack 2 with 12 rows) while each row contains 144 pads in ϕ-direction. The large number of pads in a row leads to a large granularity in y-direction, which is necessary for a fine resolution measurement of the transverse momentum by the Lorentz deflection in y-direction. As every MCM reads out 21 channels (from which three are shared with the neighbouring MCM) this leads to a number of 128 (96) MCM's in one module on 8 (6) ROB's controlled by a **D**etector **C**ontrol **S**ystem (DCS) board.

Tilted Pads

To improve the resolution in z-direction which is generally limited by the small number of pad rows in comparision to the ϕ-direction, the pads are tilted by ±2° whith the

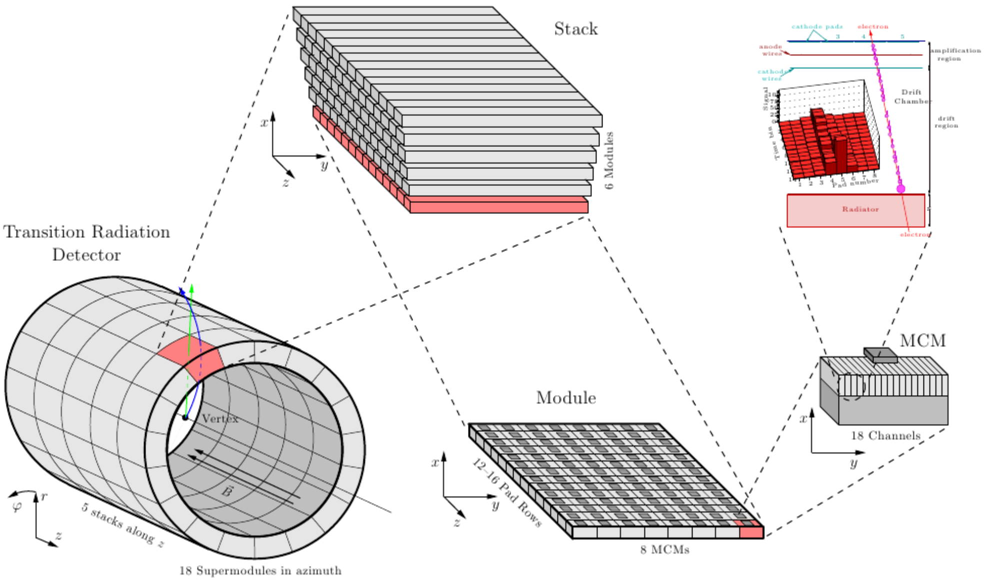

Figure 3.2: An overview of the structure of the TRD [dC08]

sign changing by layer (fig. 3.3). Considering the deviation of the original to the now processesed position alternating with the layer number, the z position can be calculated more precisely. As a consequence also the measured angular position has to be corrected with respect to the z-position.

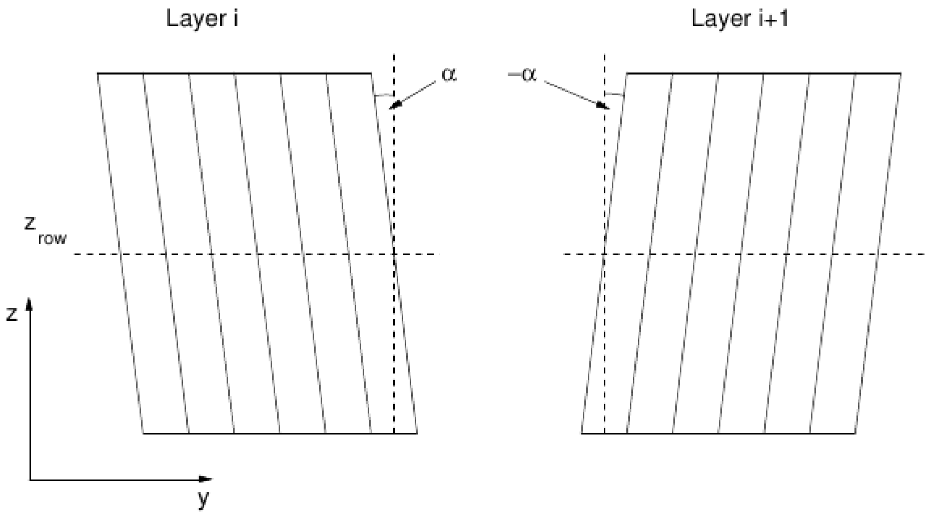

Figure 3.3: Geometry of the tilted pads [Col01]

3.3 Read-Out Electronics

Every MCM on the ROBs contains a **P**re-**A**mplifier and **S**haper **A**mplifier (PASA) and a **T**racklet **P**rocessor (TRAP), while the TRAP itself is a composition of an **A**nalog to **D**igital **C**onverter (ADC), converting the PASA output to a 10 bit digital signal with a sampling rate of 10 MHz and an output of $\pm 1\,\mathrm{V}$, a **T**racklet **P**re-**P**rocessor (TPP) to filter the data and then search for possible hits and four MIMD CPUs[1]. Besides the signal filters in the TPP the TRAP chip also applies signal corrections like the pad response function, the lorentz correction and the correction of the tilted pads which will be discussed in section 4. Many parameters for the data processing can be configured and stored into registers in the TRAP chip (section 5).

The calclulated tracklets are shipped to the Global Tracking Unit (GTU), which selects tracklets of different layers belonging to the same track of a particle. It then calculates the approximately linear direction of the track, using its offset to the interaction point as a fast estimation of the particles p_T and sends its information about the L1 Trigger to the CTP. If the event is accepted by the L1-trigger, the data is forwarded to the HLT and DAQ. The full scheme of of the electronic data flow is shown in figure 3.4.

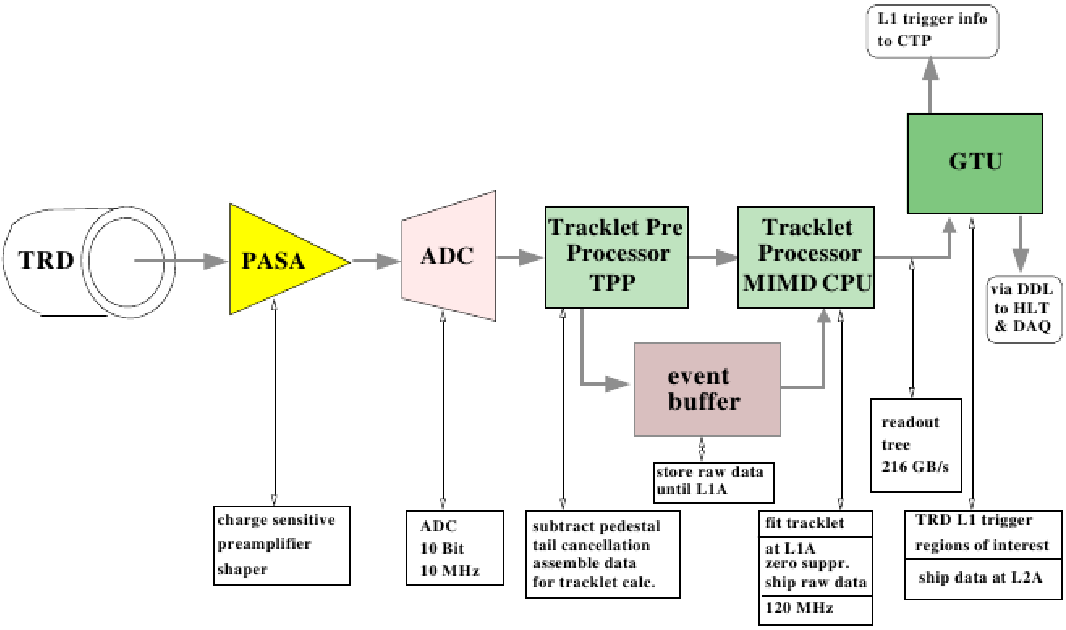

Figure 3.4: A sketch of the signal flow from the PASA to the **G**lobal **T**racking **U**nit (GTU). The whole local tracking is configured by the TRAP-registers. The found tracklets are shipped to the GTU, while the raw data is buffered to wait for the L1-Trigger accept. The creation and saving of raw data before the tracklet fitting allows an additional later tracklet calculation during the reconstruction of the raw data. [Col01]

---

[1] MIMD means Multiple Instruction stream, Multiple Data stream and refers to a multiprocessing technique used for a fast calculation of the tracklets in this case. [MIM04]

3.4 Trigger System

The TRD electronics is designed to contribute to the L1 trigger by evaluating several trigger conditions. More precisely, these are triggers on the electron-positron channel of the J/Ψ- and Υ-decay and single electrons of open charm and beauty decays by the fast and efficient PID of electrons, or for example the triggering on jets by looking for high-p_T collimated particles within the TRD stacks. The hardest challenge in the L1-trigger contribution is the maximum time available of approximately $7\,\mu$s till the L1 accept. In figure 3.5 the timing for the trigger calculations is shown. After the pre-trigger, the calculation of the tracklets in the front end electronics (MCMs) s is started and finished after approx. $3.6\,\mu$s, and then in case of a L0-accept shipped to the GTU, which performs tracking and particle identificaction and then ships the L1 signal information to the CTP. In case of the L1-accept, the buffered raw data is transfered to the GTU to wait for the L2 accept.

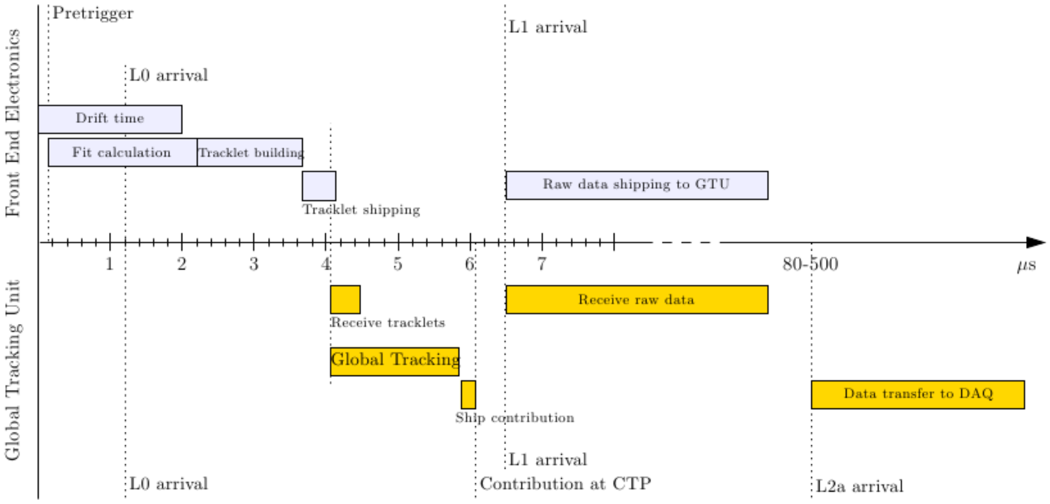

Figure 3.5: The timing of the calculations till the L1 and L2 trigger [Kle08]

3.4.1 Jet Trigger

As indicated, the trigger system of the TRD can be used as a jet trigger. For this case, the GTU fits the track slopes for the particles and calculates their p_T. Then it tries to find tracks above a specified momentum cut $p_{T,min}$ within the TRD stacks. If one module contains at least n_{min} charged tracks than a pre-defined threshold, the GTU accepts this event to possibly contain a jet and fires the corresponding L1 Trigger signal. By now hadron collisions and the jet fragmentation can be well described by Monte-Carlo models, so that by an analyis on the Monte-Carlo level one can achieve an estimate of the potential performance of such a trigger at different particle and momentum thresholds, which is shown in the following.

Proton-Proton Jet Trigger

The comparatively low multiplicity in proton proton collisions and thus the distinct jets relative to the background provide a good basis for a well working jet trigger. With the help of PYTHIA, one of the worlds most used generators for hadron collisions, it is possible to generate a set of events with each containing jets (Jet-Jet events) and also minimum bias data, which unburderns the analysis as one can split it up easily to a part for the jet efficiency and another part for the rejection of minimum bias events.

At first, about 700000 jet-jet events[2] at $\sqrt{s} = 7\,\text{TeV}$ are used to determine the efficiency of a Jet Trigger depending on the jet energy at the MC level. To ensure enough statistics for each jet energy, the events are created in 10 $p_{t,Hard}$ bins (table 3.1), which means that PYTHIA sets the initial hard scattered parton which is the origin of the jet within a certain p_T-range. To ensure the events of the different bins can be merged later on, the information about the jet production is stored, containing most notably the total cross section for jet production in *pp* and the number of trials, which PYTHIA needed to create the asked event and information on the jet quantities like jet energy and axis. The used $p_{T,hard}$-bins in this production are listed in table 3.1. To obtain the trigger efficiency, the TRD geometry is approximated by ideal stacks with no dead zones, each with an extent of 0.36 in η and 0.35 in ϕ. In each event, the charged Monte-Carlo physical primary particles above $p_{T,min}$ per stack are counted. If one stack counts more particles than n_{min}, the event is marked as triggered.

Table 3.1: Used $p_{T,hard}$ bins. The lower boundary of each bin range is given in the row "min $\mathbf{p_{T,hard}}$" while the upper one is given by the lower boundary of the next bin.

$\mathbf{p_{T,hard}}$ **bin**	1	2	3	4	5	6	7	8	9	10
min. $\mathbf{p_{T,hard}}$ **[GeV]**	5	11	21	36	57	84	117	156	200	249 (- 1000)

In figure 3.6 the trigger efficiencies are presented for different n_{min} and $p_{T,min}$ dependent on the leading jet p_T of the jets within the TRD acceptance. Events with no jets within $|\eta| < 0.9$ are sorted out. The efficiency was calculated by dividing the leading jet spectrum of triggered events by the spectrum of all events. It can be observed, that thresholds of $p_{T,min} = 4$ or $n_{min} = 4$ clearly are too high as they suppress to many jets. For the other threshold combination the efficiencies seem quite reasonable, as one has to consider that the real online efficiency will be worse due to dead zones and other effects.

For a better estimation of the right thresholds, the suppression of minimum bias events is even more important if one considers the high interaction rate at *pp* runs. For this, a PYTHIA minimum bias production (LHC10f6a) at $\sqrt{s} = 7\,\text{TeV}$ has been taken and analysed with the same conditions. As the jet energy is not a reasonable quantity any

---

[2] production LHC10e14, More information about the prodcutions can be obtained at MonALISA (`http://alimonitor.cern.ch`)

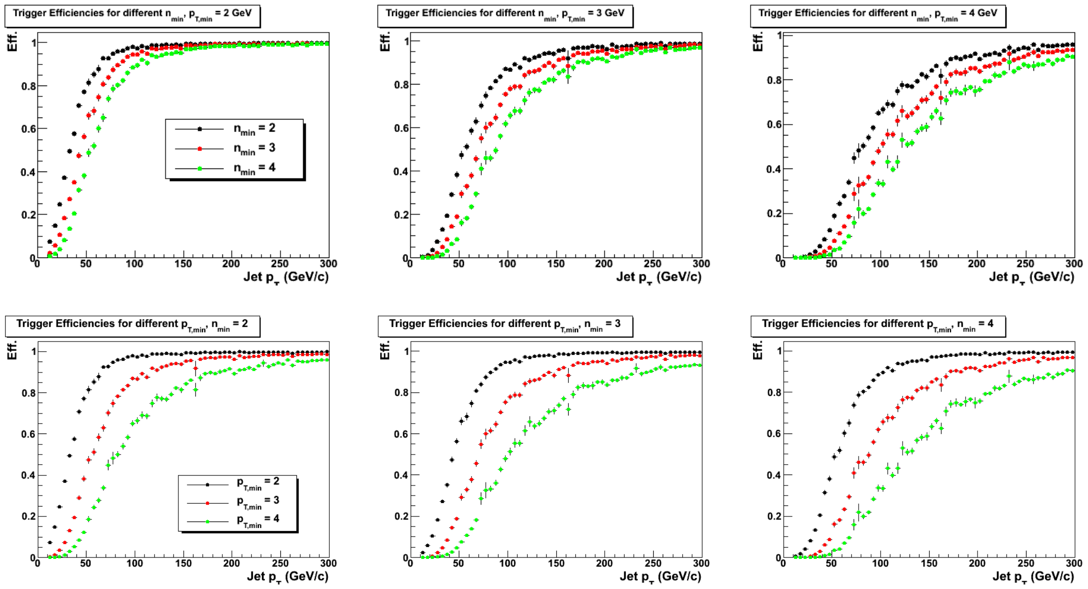

Figure 3.6: Trigger Efficiencies depending on jet energy. In the upper three plots, always the $p_{T,min}$ cut is fixed, in the lower three n_{min}. The jet energy has been taken directly by PYTHIA event information stored during the generation.

more, the number of physical primary monte carlo particles (resp. multiplicity) has been chosen as the new x-axis. The results are shown in figure 3.8. One can clearly observe the raise of the trigger efficiency with increasing multipclitiy. In addition, the overall trigger rejections (inverse efficiency) have been calculated. The results are displayed in figure 3.7 and table 3.2. It is quite obvious that a change of n_{min} for triggering has a very strong effect on the rejection considering it is only configurable in integers and should therefore be treated carefully, as the same results can be achieved by changing $p_{T,min}$, which can be set much more precisely.

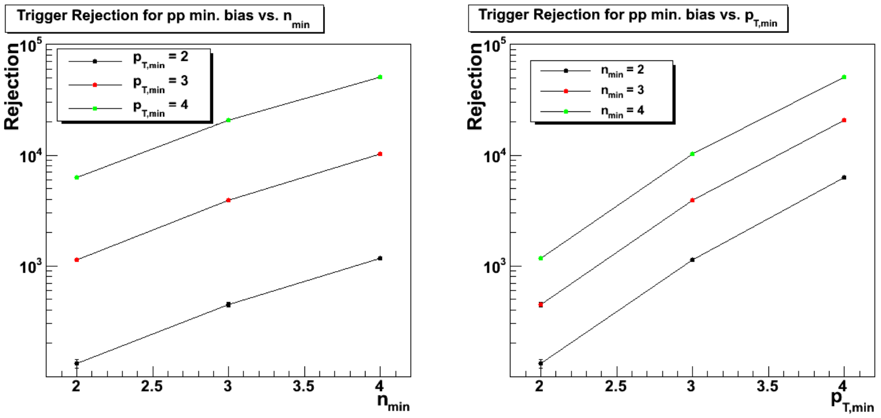

Figure 3.7: Rejection of a jet trigger for pp min. bias events vs. $p_{T,min}$ and n_{min}

Table 3.2: Rejection of a jet trigger for pp min. bias events.

pp	2 Particles	3 Particles	4 Particles
2GeV	131 ± 11	445 ± 21	1180 ± 30
3GeV	1140 ± 30	3920 ± 60	10300 ± 100
4GeV	6270 ± 80	20800 ± 100	50800 ± 200

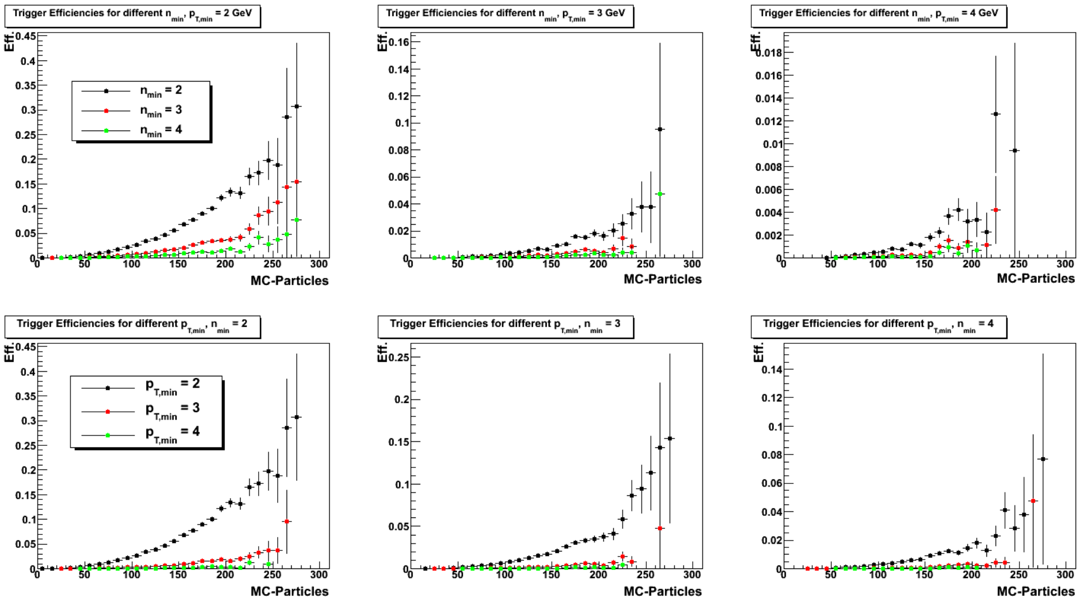

Figure 3.8: Trigger Efficiencies depending on multiplicity for mb events.

4 Online Tracklet Calculation and Tracking Procedure

4.1 General Idea

As full track reconstruction concerning track curvature and energy loss requires complex algorithms which can impossibly be handled in the short time left for the GTU to calculate PID and the track's p_T, a simple way to estimate these quantity is mandatory. The TRD solves this problem by calculating small track segments in the 6 layers, fitting them together to a long track segment in the TRD using only linear fit algorithms for the tracklets and the TRD track segment.

In the first step, the data is digitized and then filtered (section 4.3). After that, the TRAP searches for clusters which comply with certain quality thresholds (section 4.4.2) and finally the systematic deviations are corrected (section 4.5).

4.2 Local Coordinate System

For further explanations and for a better understanding of the tracklet calculaction procedure it is useful to change into a local cartesian coordinate system, as every module has a consimilar straight geometry, were the spherical coordinate system of the ALICE detector would just be obstructive. The local coordinate system is shown in figure 4.1. The z-axis

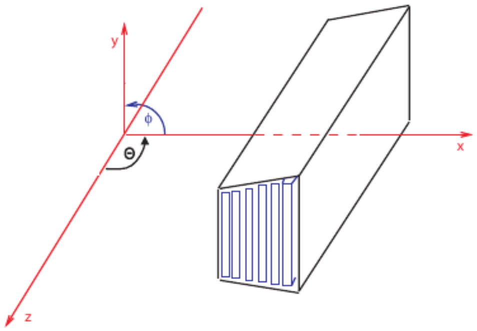

Figure 4.1: Local coordinate system for the TRD modules

of the new coordinate system represents the beam axis, while the x-axis specifies the distance from the interaction point and intersects a chamber in the center. Thus the y-axis states the distance from the chamber center in $r\phi$-direction.

4.3 Digitization and Filtering

In the very first step, the data needs to be digitized by the ADC's. The amount of deposited charge is availiable for each ADC channel and time (at a sampling frequency of 10 MHz the time information is available in timebins of 100 ns) per MCM. The digitized data of a traversing charged particle recorded in an MCM[1] is visualised in the left panel of figure 4.2.

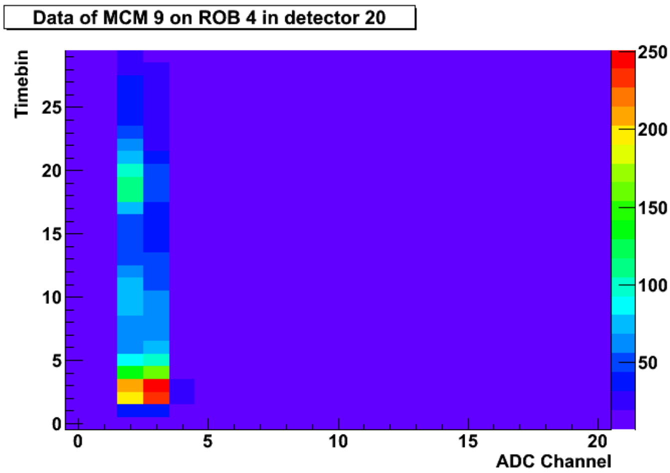

Figure 4.2: 2-dimensional plot of the deposited charge within the timebins of the ADC channels of a traversing particle. The amplification peak is clearly visible, also one can observe that the charge is deposited on several neighbouring pads within the same timebin (section 4.4.1).

The digital information of charge/timebin is now filtered as described below ([Col01], [Gut02], using $I(t)$ to name the incoming signal and $O(t)$ as the outcoming signal of a single filter stage.

4.3.1 Non-linearity Correction Filter

$$O(t) = I(t) \cdot 4 + \mathrm{LUT}_{\mathrm{NL}} \frac{\mathrm{I(t)}}{16} \tag{4.1}$$

The non-linearity filter uses a given editable look-up table ($\mathrm{LUT}_{\mathrm{NL}}$) stored within the TRAP-chip to correct non-linear variations in the electronics. The multiplication by 4 adds two binary fractional digits to avoid rounding errors in the further signal calculation.

---

[1] Data from a simulation

4.3.2 Pedestal Correction Filter

$$O_n(t) = I_n(t) + P_{NP} - P_n(t) \tag{4.2}$$

For each ADC channel n the pedestal P_n is determined by a relaxation process shown in equation 4.3 and 4.4, and then a nominal pedestal P_{NP} is added. Thus later in the signal chain the nominal pedestal value is the same known one for every channel and needs not to be calculated any more.

$$\begin{aligned} P_n(t) &= P_R(t) \qquad (4.3) \\ P_R(t+1) &= P_R(t) + (I(t) - \beta \cdot P_R(t)) \qquad (4.4) \end{aligned}$$

4.3.3 Gain Correction Filter

$$O_n(t) = \gamma_n \cdot I_n(t) + \rho_n \tag{4.5}$$

The gain correction filter is adjustable for each ADC channel. The scaling factor γ_n allows a correction of pm 12 % of individual electronics or gas gain related variations. The additive ρ_n corrects scaling related baseline shifts.

4.3.4 Tail Cancellation Filter

$$O(t) = I(t) - S(t) \tag{4.6}$$

The tail cancellation filter substracts the signal $S(t)$ caused by the ion tail of the gas chamber from the input signal. The function $S(t)$ can be approximated by a superposition of two exponentials [Gut02] shown in equation 4.7 and 4.8. The parameters α_L, λ_L and λ_S can be configured within the TRAP chip.

$$\begin{aligned} S(t) &= \mathbf{1}_{t\geq 0} \cdot \sum_{n=1}^{2} \alpha_n \cdot e^{-\kappa_n t} + R_2(t) \qquad (4.7) \\ S(t) &= \mathbf{1}_{t\geq 0} \cdot \left[\alpha_L \lambda_L^t + (1-\alpha_L)\lambda_S^t\right] \qquad (4.8) \end{aligned}$$

4.3.5 Crosstalk Suppression Filter

The purpose of the crosstalk suppression filter is to correct correlations between neighbouring ADC channels. However, there seems no need to use it at the moment.

4.4 Tracklet Calculation

After the application of the digital filters, the signal is passed to the TPP which detects the hits, determines the clusters and finally calculates the tracklets. Therefore several conditions need to be applied to improve the signal-to-noise ratio of the detected tracklets and also the corresponding resolutions.

4.4.1 Hit selection

First, possible hits have to be found. For every timebin the TPP looks for local maxima of depositited charge $Q_i(t)$ in the ADC channels and then calculates the sum $Q_{Cluster}$ with the neighbouring channels (clusters)

$$Q_{Cluster}(t) = Q_i(t) + Q_{i+1}(t) + Q_{i-1}(t) \quad . \tag{4.9}$$

To provide a quality condition to exclude noisy charge contributions, the TPP requires Q_{Cl} to be above a certain selectable threshold T_{Cl}. Since the cluster detection works after the filtering process, T_{Cl} is sensitive to the settings of the different filter steps, which affect the signal in different ways (pedestal value, tail cancellation, etc.). Only accepted clusters are used for the tracklet calculation. In addition, the following cluster verification threshold T_Q can be applied to remove overlapping clusters

$$\frac{Q_{i+1}(t) \cdot Q_{i-1}(t)}{Q_i^2} < T_Q \quad . \tag{4.10}$$

To provide a better position resolution of the clusters than the pad width, the cluster position is corrected with a position look-up table created with help of the pad response function explained below.

The Pad Response Function

Naively the position resolution is limited to the pad length ($\approx$ 7.5 cm - 10.1 cm) and width($\approx$ 0.65 cm - 0.80 cm). The position resolution in the direction of the pad length is improved at the GTU level by tilting the pads while the resolution in direction of the pad width can be corrected by assuming a nearly gaussian cluster deposition called **P**ad **R**esponse **F**unction (PRF) on two to three pads [Wul09]:

$$PRF(y) = \frac{Q_i(t)}{Q_{Cluster}} \approx A \cdot e^{\frac{y^2}{2\sigma^2}} \tag{4.11}$$

The resulting PRF is shown in figure 4.3. With the knowledge of the charge distribution on the pads and the PRF now the mean position y can be calculated.

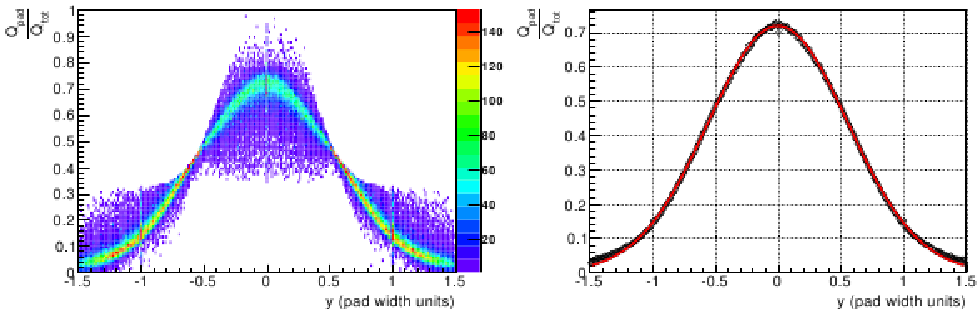

Figure 4.3: The measured PRF (left) and then averaged and fitted PRF (right) for the padwidth of 6.95 mm. [Wul09]

4.4.2 Tracklet Conditions

After applying the position correction with the PRF, the TPP looks channelwise for tracklet candidates. If it finds a specified number of clusters $T_{C,L}$ for a channel in a given timebin window $[t_s, t_e]$, it checks the following channels if the value of all contributing clusters exceed a pre-defined threshold $T_{C,T}$. All four conditions can be written directly into the TRAP hardware. If the conditions are fulfilled (also if more than one tracklet is found), the MIMD preprocessors within the MCM will calculate a straight line fit through the found clusters and store the information of the y-position, the deflection dy, the pad row / z-position and the PID information in the “tracklet word” (section 5.2).

4.5 Position and deflection corrections

The calculated tracklet slope dy- and the y-position need to be corrected due to systematic effects and structural design and restrictions. The position improvement with the PRF was already explained above, so with the tilted pads and the lorentz drift for an applied magnetic field two corrections are left to be discussed.

4.5.1 Pad Tilting

The tilted pads (explained in section 3.2) provide a better resolution in z-direction (after the corresponding calculations), but also lead to a deviation of the real y- and measured y-position and affect the measured deflection, too (fig. 4.4). Thus, both need to be corrected. Since each MCM can only determine the z-position with a granularity of pad rows, it can not be corrected directly by the MCM and is therefore done in the GTU, while

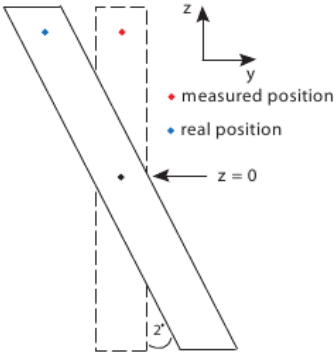

Figure 4.4: The real position on the tiltet pad in comparision to the measured position with no tilting considered [Wul09]

the deflection can be directly calculated without knowledge of a more precise z position, as only the position of the pad is needed (sections 6.1.1 equations 6.3 and 6.4).

4.5.2 Lorentz Correction

With the application of a magnetic field one has to deal with a systematic shift of the measured deflections, as the drifting electrons within the gas chamber are Lorentz deflected themselves by the magnetic field. The effect is outlined in figure 4.5. The slanted drift direction of the electrons leads to a shift of the tracklet angle and therefore the measured deflection. The angle between the perpendicular drift direction and the slanted one is called Lorentz angle Ψ_L and can be calculated by

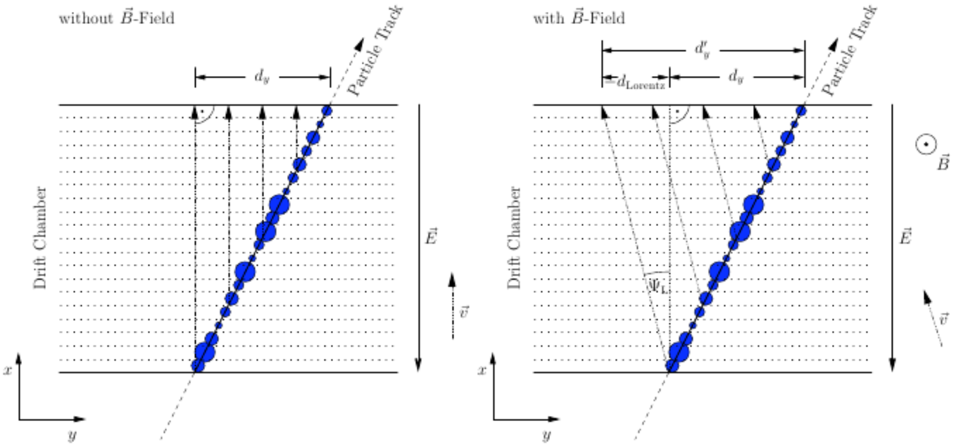

Figure 4.5: *Left:* The electron drift after a particle hit without a magnetic field. *Right:* The applied magnetic field leads to a slanted drift of the electrons.[Kle08]

$$\tan \Psi_L = \omega \tau \tag{4.12}$$

where $\omega = \frac{e}{m}B$ is the cyclotron frequency and $\tau = \frac{m}{e}\mu$ the mean time interval between two collision of the electron with the gas. The electron mobility μ is given by $\mu = \frac{v_{Drift}}{E}$, and therefore equation 4.12 can be written as

$$\tan\Psi_L = \omega\tau = v_{Drift}\frac{B}{E} \tag{4.13}$$

which clearly shows the dependency of the lorentz angle on the magnetic field B and the electric field E. The deflection correction, which can be stored in each MCM seperately, relies on the knowledge of these quantities.

5 Software Description

To simulate the events with full implentation of the TRD electronics and geometry responding on the generated particles, the softwarte AliROOT has been used. AliROOT is based on the ROOT analysis framework, a powerful object orientated C++ Interpreter containing predefined classes for histograms, fitting and other common analysis tools [ALI11]. In AliROOT, classes considering the set-up of the ALICE detector including detector funcionallity and the whole ALICE geometry for the simulation had been added. The AliROOT software is continually in development; classes providing fast access on physical variables are programmed and existing ones are improved. For the analysis in this thesis the momentary trunk[1] version (Rev. 46704) has been used.

5.1 General Architecture

The AliROOT software has been designed to operate on raw event data from LHC runs as also on simulated event data. In general, the analysis is performed on so called ESD files, the final step of compressed event data, containing reconstructed tracks and other important information about the event. To gain the ESD information, the data has to be reconstructed out of the online raw event or the offline simulated Monte-Carlo data. The scheme of data evolution is shown in figure 5.1.

As one can see, the reconstruction can run on the raw data of the recorded events from LHC real data, but also on the so called “Digits” produced by Monte-Carlo simulations. Besides, the digits can also be transformed into the same raw format like the real data.

Besides the ESD files (`AliESDs.root`) several files which are created during the simulation are of greater interest for the later analysis. In `Kinematics.root` the MC information about all simulated particles of the event is stored (even if they are not reconstructed). This information is complemented by the `DET.TrackRefs.root` files (DET must be replaced by the desired detector’s token, e.g. TRD) where the MC track references are stored. They provide information about an MC particle’s state when entering the detector or the like. In addition, the full simulation information for the TRD tracklets is also stored in `TRD.Tracklets.root`.

---

[1] Version currently in development

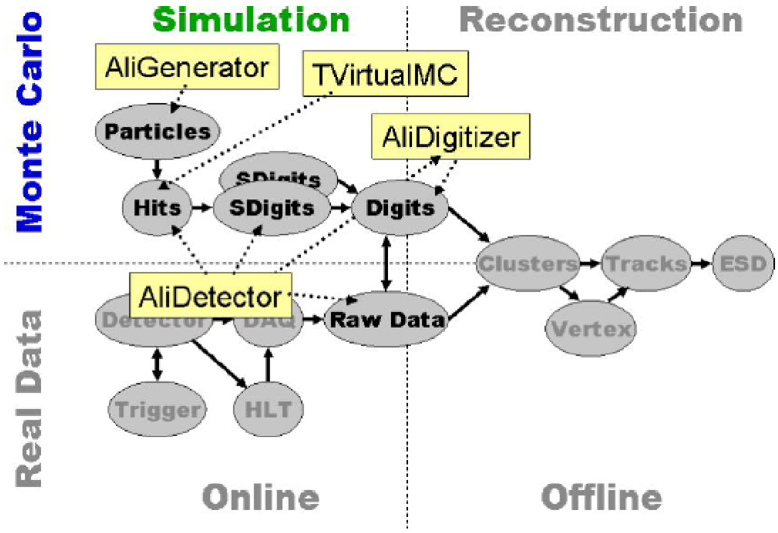

Figure 5.1: Schematic view of online on offline procedures within aliroot for real and simulated data. [ALI11]

5.2 Simulation of the TRD

Every detector's electronics and read-out scheme is fully simulated for almost each single component used and so provides a data flow close to the online operating detectors. For the TRD, this means a full simulation of the TRAP-chip and the GTU. A list of all necessary classes for the TRD simultation would go beyond the scope of the thesis, so the focus lies on the most important classes needed.

`AliTRD`. This class is the base class of the TRD simulation environment. It provides the functions to set the subclasses to work and to get references to for example the TRD geometry.

`AliTRDgeometry`. All geometrical information is modeled with this class. It offers the possibility to remove modules from the simulation and also to get pointers to classes containing pads or the like. Also the dimensions of certain modules and pad planes can be accessed.

`AliTRDcalibDB` Basic information about the calibration can be accessed via this class which takes its information out of the OCDB. It is used to get information about the PRF or the drift velocity within the chambers.

`AliTRDCommonParam` and `AliTRDSimParam`. These classes provide information about the parameters of the TRD, while `AliTRDCommonParam` focusses on general parameters like the gas mixture etc. and is therefore also used for reconstruction, while `AliTRDSimParam` focusses on the simulation parameteres like the filter settings, which are set via the `AliTRDtrapConfig` class or the like.

`AliTRDtrapConfig`. As indicated in section 4 the TRAP chip has got several registers containing assignable values for the data processing within the filters and the tracklet calculation. These can also be set within the simulation in this class. The table in figure 5.1 shows the register names and default values for the different assignable parameters used and changed during the following analysises.

`AliTRDmcmSim` This class fully simulates the MCMs on the ROBs.

`AliTRDtrackletWord` and `AliTRDtrackletMCM`. These classes hold the tracklet information. While `AliTRDtrackletWord` holds the tracklet raw data from the detector (y, dy, z, PID), `AliTRDtrackletMCM` additionally stores data from the simulation like the corresponding track label or the quality of the linear fit.

For the analysis the tasks `AliTRDonlineTrackletFilter` and `AliTRDonlineTrackletQA` have been used and modified to extract the tracklets out of the `TRD.Tracklets.root` file and to obtain basic position and deflection information.

Table 5.1: Default filter settings used for the start with corresponding TRAP register names as configurable online within the TRAP chip [Kle11], [Wal10]. For the tail cancellation two sets of parameters had been applied.

Filter	**Parameter**	**Reg. Name**	**Default**
Non-Linearity Correction	Look Up Table	FLLn	$\mathrm{LUT}_{\mathrm{NL}}$
Pedestal Correction	Time Constant	FPTC	2
	Correction Additive ($P(t)$)	FPNP	$4 \cdot 10 = 40$
Gain Correction	Factors (γ_n)	FGFn	*Bypassed!*
	Additive (ρ_n)	FGAn	*Bypassed!*
Tail Cancellation	Long Decay Weight (α_L)	FTLA	246 / 200
	Long Decay Parameter (λ_L)	FTLL	258 / 200
	Short Decay Parameter (λ_S)	FTLS	211 / 0
Preprocessor			
Tracklet Fitting	Fit Start	TPFS	3
	Fit End	TPFE	20
	Candidate Left	TPCL	4
	Candidate Right	TPCT	12
Charge Accumulation	Start Window 0	TPQS0	1
	End Window 0	TPQE0	8
	Start Window 1	TPQS1	8
	End Window 1	TPQE1	20
Cluster Detection	Cluster Threshold	TPHT	240
	Cluster Quality Threshold	TPVT	*Bypassed!*
	Effective Pedestal	TPFP	40

6 Tuning of the Tracklet Calculation and Filter Settings in Simulations

The most important information of the tracklets is their deflection dy, their position y in local coordinates and their information about PID. This thesis is focused on the tracklets deflection and the position quality and efficiencies for simulated tracklets with different filter settings (especially for the tail cancellation) and (non-)presence of the solenoid field of 0.5 Tesla. As the local position and momentum of Monte-Carlo tracks can be directly accessed at TRD level by the track references, it is not necessary to simulate the full ALICE detector geometry but only the Transition Radiation Detector. First of all this saves time for the simulations and also prevents the loss of particles before the TRD due to interactions with the other detectors and detector frames. Also, as PID is not rather important for this thesis, the generated events consisted of 10 protons and anti-protons at a momentum of 10 GeV randomly fired in to the TRD from the centre of the barrel, which will not cause TR and therefore have a more simply pulse height spectrum. If not otherwise specified, the number of generated events of this type was 500.

6.1 Applying Corrections

In the following, mainly two quantities are studied. These are the position and the deflection residuals of the tracklets to Monte Carlo track references Δy and Δdy, defined in equation 6.1 and 6.2.

$$\Delta y = y_{Trkl} - y_{MC} \tag{6.1}$$

$$\Delta dy = dy_{Trkl} - dy_{MC} \tag{6.2}$$

To obtain a value for the resolution of y and dy, the residuals are fitted with a gaussian function. As all of the corrections except for the correction of the Lorentz angle Ψ_L are not addicted to a presence of the magnetic field, they are done without a solenoid field. The tail cancellation was found to have a very high impact on the signal strength and therefore also on the number of found tracklets, so it was disabled to simplify the situation at first and for a later comparison. The gain correction stayed disabled during the whole thesis as the simulated data is clean of electronic or gas gain variations anyways . Generally the default settings for the TRAP chip shown in table 5.1 have been used for the tracklet simulation.

6.1.1 Correction of the Tilted Pads

To correct the systematic deviations due to the pad tilting, one has to adjust the position of the monte carlo track references, as a single MCM is not capable of these correction because of the unkown real z-position.

So, y_{MC} is adjusted to the tilting deviations as following with $\alpha_{tilt} = 2°$ and the the layer number L (starting at 0)

$$y_{MC} = \tan\left[(-1)^L \cdot \alpha_{tilt}\right] \cdot (z_{MC} - z_{trkl}) \quad . \tag{6.3}$$

For the deflection correction the knowledge of the real z position is not important. Thus it can be directly done by the TRAP chip, where the whole deflection correction (including the lorentz correction) can be stored for each MCM. The correction needed for dy is given by

$$dy_{tilt} = dx \cdot \tan\left[(-1)^L \alpha_{tilt}\right] \frac{z_{trkl}}{x_L} \quad . \tag{6.4}$$

In figure 6.1 the influence of the position and deflection correction due to the pad tilting is shown.

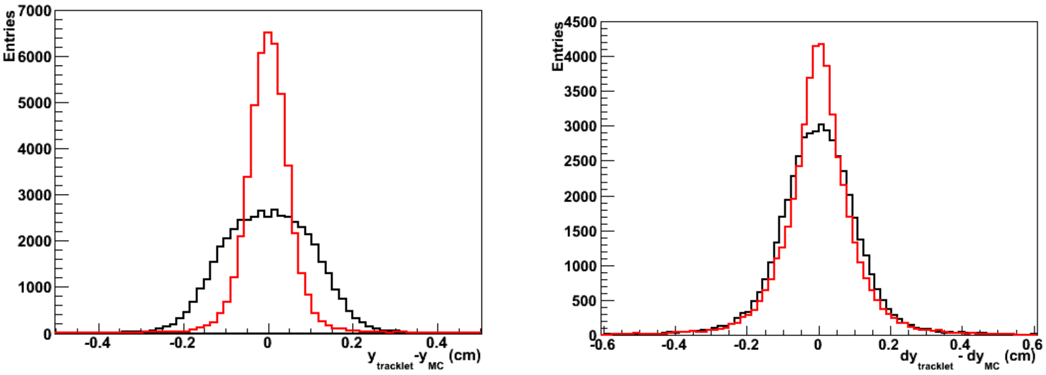

Figure 6.1: Residuals of position (left) and deflection (right) after applying the correction for the tilted pads (red) in comparision to the uncorrected distribution (black), $B = 0\,\mathrm{T}$

The resolution of the position and deflection is clearly improved by considering the tilting angle.

6.1.2 Resolution Improvement with the PRF

After the tilted pads are corrected, the resolution in y direction is being improved by the PRF according to section 4.4.1. Therefore, the center of gravity is calculated for the cluster charge in the three contributing ADC channels by

$$\mathrm{COG} = \left| \frac{\mathrm{Q}_{\mathrm{i+1}}(\mathrm{t}) - \mathrm{Q}_{\mathrm{i-1}}(\mathrm{t})}{\mathrm{Q}_{\mathrm{i}}(\mathrm{t})} \right| \quad . \tag{6.5}$$

The center of gravity for the PRF can be calculated similar for any y position with

$$\mathrm{COG(y)} = \left| \frac{\mathrm{PRF(y+1)} - \mathrm{PRF(y-1)}}{\mathrm{PRF(y)}} \right| \quad . \tag{6.6}$$

The real y position can be now reconstructed by looking up the corresponding y position calculated with the PRF for the COG of the three channel charges. As the PRF is symmetric, this can be realised by a look-up table which stores the COG(y) for the y-values so that the position can be calculated by [Kle08]:

$$y = \frac{1}{2}\mathrm{COG} + \mathrm{LUT}_{\mathrm{PRF}}(\mathrm{COG}) \tag{6.7}$$

As the pads are wider for the outer layers of the TRD, the effect is the strongest there. To show the influence of the correction with the PRF well, Δ_y has been plotted vs. y_{MC} in figure 6.2 for the outermost layer. With no PRF correction, the calculated tracklet position systematically differs if the MC-position is not within the pad center. It is therefore expected, that the PRF has an obvoius influence on the final position and deflection resolution, which is shown in the residual plots in figure 6.3. Evidently the resolutions have been slightly improved.

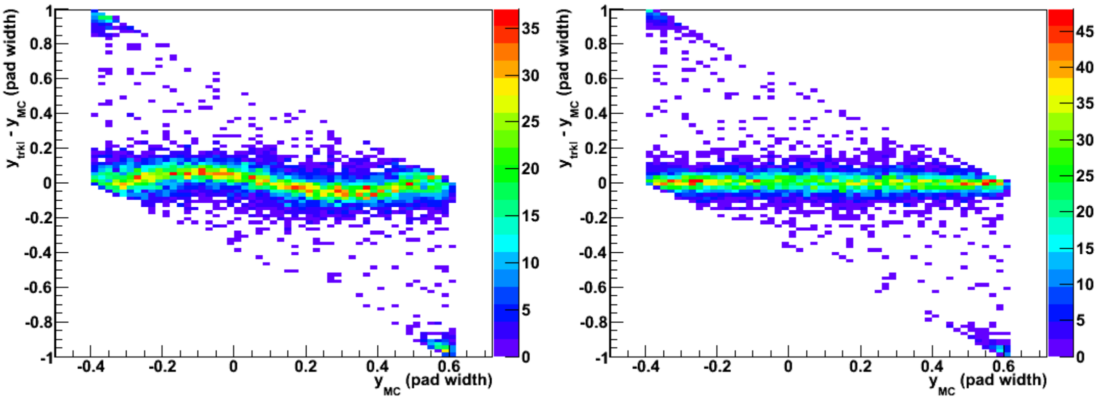

Figure 6.2: The position residuals as a function of the Monte-Carlo position. *Left:* No position correction with the PRF applied. *Right:* Corrected positions via the LUT. $B = 0\,\mathrm{T}$

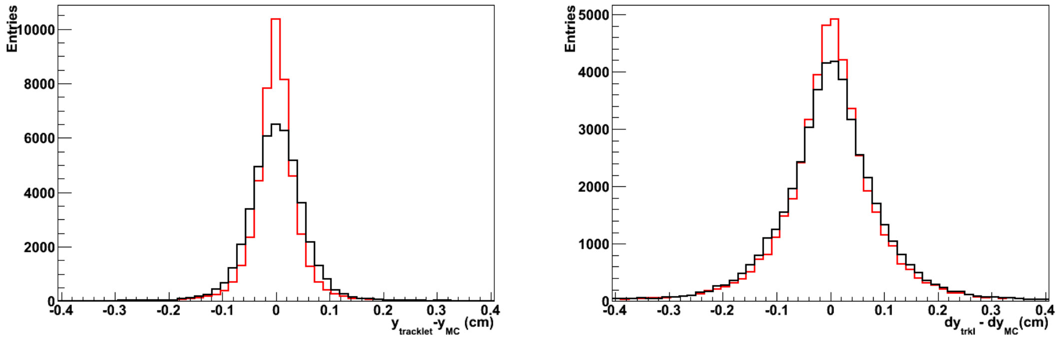

Figure 6.3: *Left:* Position residuals before (black) and after (red) application of the PRF correction. *Right:* same for the deflection residuals. $B = 0\,\mathrm{T}$

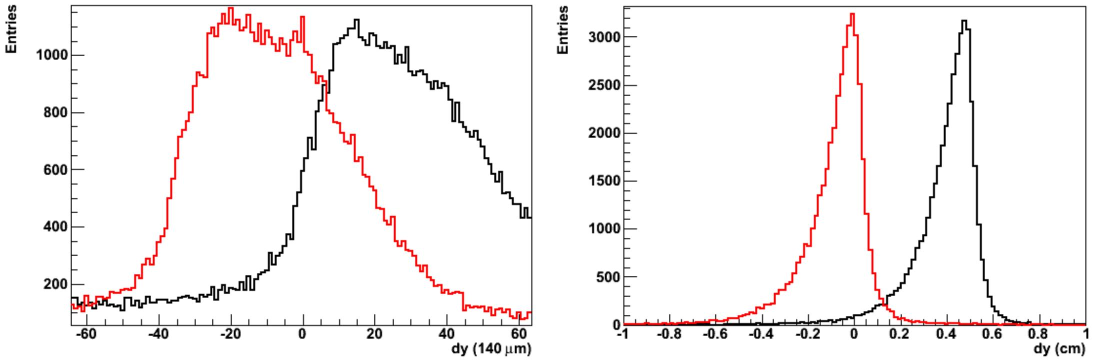

Figure 6.4: Deflection and deflection residuals before (black) and after (red) the lorentz correction. $B = 0.5\,\mathrm{T}$

6.1.3 Lorentz correction

Already mentioned in section 6.1.1, the correction of the deflection can be stored within each TRAP chip. The total deflection correction is the sum of the actual tilting and lorentz correction. Since the measured deflection dy' is given by

$$dy' = dy_L + dy \tag{6.8}$$

with the lorentz deflection dy_L and the real deflection dy, one can easily calculate the real deflection by the knowledge of $\omega\tau(0.5\,\mathrm{T}) = 0.167386$, which can be obtained by the TRD simulation classes for every TRD chamber[1], since dy_L is calculated with the drift length $x_{drift} = 3\,\mathrm{cm}$ by:

$$dy_L = \tan \Psi_L \cdot x_{drift} = \omega\tau \cdot x_{drift} = 0.502\,\mathrm{cm} \tag{6.9}$$

The urgent need of the Lorentz correction is shown in figure 6.4, where just the PRF and tilting corrected dy and Δdy distributions are compared. One can observe the clear

---

[1] However, the simulation provides the same $\omega\tau$ for all chambers

deviation of about 0.5 cm between the uncorrected and corrected distributions. The still asymmetric shape of the residual distribution which occured after applying a magnetic field has another origin and will be explained and corrected in section 6.2.1.

6.2 Filter and Preprocessor Settings without Tail Cancellation

6.2.1 Adjustment of the Drift Time

The drift time of the electrons ionized by a particle passing the detector pads can be set within the trap chip. Theoretically, the drift time should be $t_{drift} = \frac{v_{drift}}{s_{drift}} = 2\,\mu\text{s} =$ 20 timebins but in practice the time response of the pads lead to a prolonged charge deposition which on the other hand rotates the tracklets in x direction and thus has a systematic effect on the deflection. The systematic effect is shown in figure 6.5. In the case of an applied magnetic field, it's impact leads to a shift of the residuals, while with no field applied, it widens up the residual distribution and is therefore not that obvious as in the first case. To visualize it anyway, in figure 6.6, Δdy vs. dy_{MC} is plotted which clearly shows a dependency of Δdy from dy_{MC} for both cases. Now, to find the correct drift time, the projection of the mean values of Δdy vs is fitted with a linear fit for every t_{drift}-timebin. The slopes gained by these fits are plottes against t_{drift} and then the intersection point is calculated again by a fit of the linear part (fig. 6.7. The calculation is done withouth the magnetic field, because the systematic shift due to the lorentz angle will distort the result and should be treated seperately. The calculated intersection point is $t_{drift} = 24.2402$ timebins. In figure 6.8 the corrected distributions for $B = 0$ and $B = 0.5T$ are shown. The calculated t_{drift} is clearly higher than the above estimated value of 20 timebins for the reasons explained above and shall thus come closer to the expected value with the application of the tail cancellation (section 6.3.1 and 6.3.2).

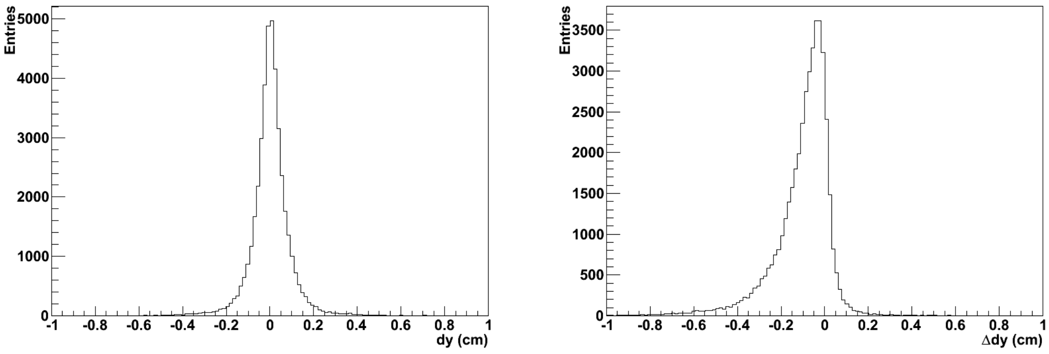

Figure 6.5: Deflection residuals. Left: No magnetic field applied. Right: Magnetic field applied.

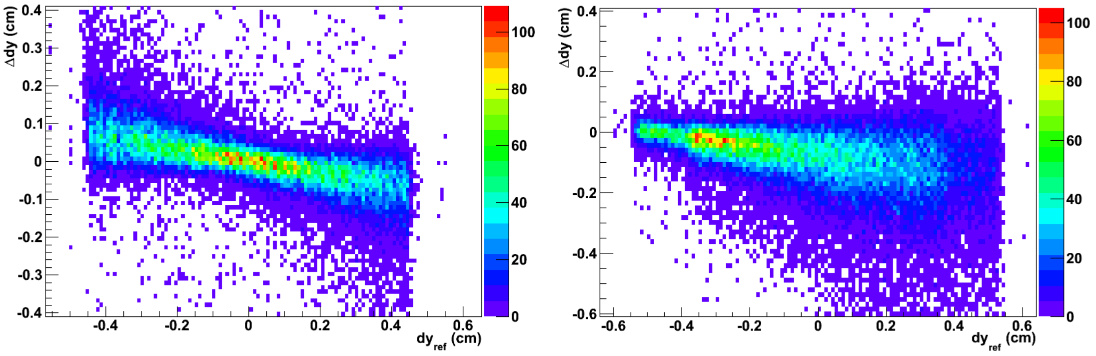

Figure 6.6: Deflection residual Δdy vs. dy_{MC}. Left: $B = 0\,\mathrm{T}$. Right: $B = 0.5\,\mathrm{T}$

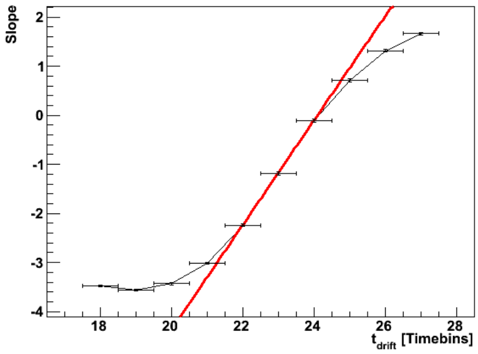

Figure 6.7: Fitted slopes as a function of t_{drift}

Now, with the applied corrections, the filter settings can be varied to study effects on the tracklet determination process. The Tail Cancellation is still switched off. Besides the resolution of the position and deflection, the **efficiency of finding a tracklet** assignable to the Monte-Carlo references of the **physical primary particles** within the TRD is determined. Tracklets which were not assigned to these track references are classified as **noise** tracklets. In addition, a simplified **tracking efficiency** is applied; MC (physical primary) particles are believed to be tracked, if a tracklet could be applied for it's track references in **4 out of 6 layers**. The quantities are chosen with respect to the GTU tracking, as a well position resolution is necessary for an accurate p_T determination and the combination of the tracklets out of the different layers is also based on the deflections [Col01],[Kle11]. The simulated tracklets can be easily assigned by the MC track label, which is the same for a particle, its track references and the corresponding simulated tracklets.

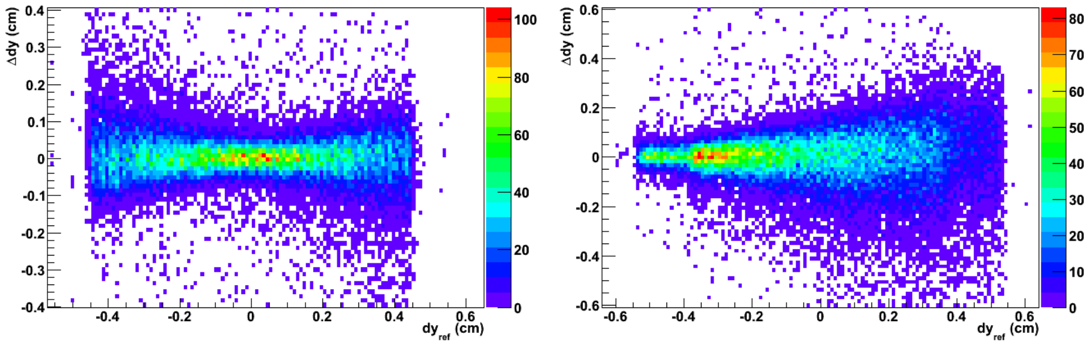

Figure 6.8: Corrected deflection residual Δdy vs. dy_{MC}. Left: $B = 0\,\mathrm{T}$. Right: $B = 0.5\,\mathrm{T}$

6.2.2 Variation of the Hit Threshhold

The hit threshold configurable in the TRAP register TPHT is one of the main settings with influence on tracklet detection. Obviously, a rising hit threshold results in the detection of less hits and therefore a loss of tracklets, but also improves a suppresion of noise. The choice of the value for TPHT depends on the chosen pedestal value. For the start, the hit threshold has been varied from TPHT = 80 to 300 in steps of 20. The analysis has been performed one time for $B = 0\,\mathrm{T}$ and $B = 0.5\,\mathrm{T}$. At first, the number of tracklets per event for different TPHTs are shown in figure 6.9 with the fraction of noise tracklets: It is obvious, that numbers below a TPHT of 140 lead to an almost overall contamination by noise tracklets. For higher values of TPHT, the number of tracklets decreases, so does the fraction of noise tracklets. Also it can be observed, that the application of the magnetic field leads to a detection of more tracklets, which seem to be mainly noise tracklets. This effect can be explained by scattered charged particles with low momentum which can be curved back into the TRD chambers several times. As these particles do not fall into the category of MC physical primary particles, their multiple tracklets will be classified as noise.

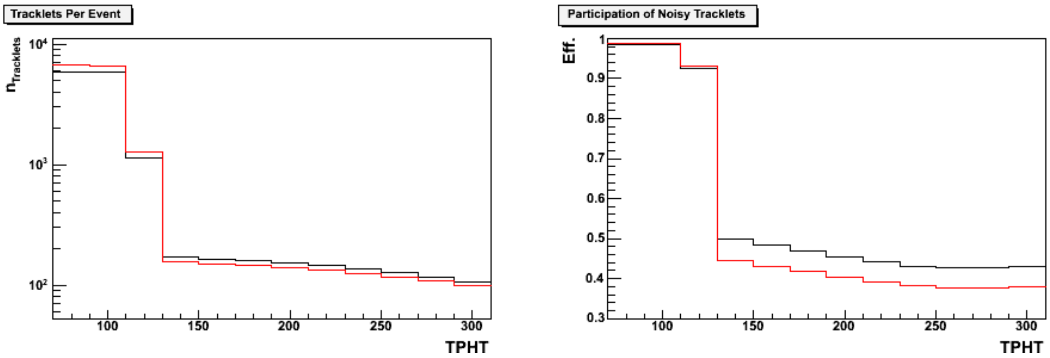

Figure 6.9: *Left:* Number of all tracklets/event. *Right:* Fraction of noise tracklets. (Red Curve: $B = 0\,\mathrm{T}$, Black: $B = 0.5\,\mathrm{T}$)

More interesting to see is, how efficient tracklets can be found, especially for the physical primaries. Therefore, the tracklet and tracking efficiencies vs. TPHT are shown in figure 6.10. There is no big difference in the efficiencies for $B = 0\,\mathrm{T}$ and $B = 0.5\,\mathrm{T}$ (except for a TPHT higher than 240), but one must notice that the efficiency for tracklet finding is almost one for low TPHT and then falling with raising the threshold, but the tracking efficiency has its maximum at ≈ 0.7 and is then falling more slowly. The explanation for this is quite simple: The track references during the simulation only belong to the TRD if the MC particles actually travels through a chamber of the TRD, and not through the space frame the whole structure is inserted in. Therefore, MC-particles traveling through the dead zones of the TRD will not contribute to the tracklet finding efficiency but to the tracking efficiency. In addition, one also has to consider the three missing stacks in front of the PHOS. To visualize this effect, the ϕ-η-distribution of lost tracks has been plotted in figure 6.11 which clearly shows, besides some lost ones within the stacks, the shape of the space frame and the three missing stacks.

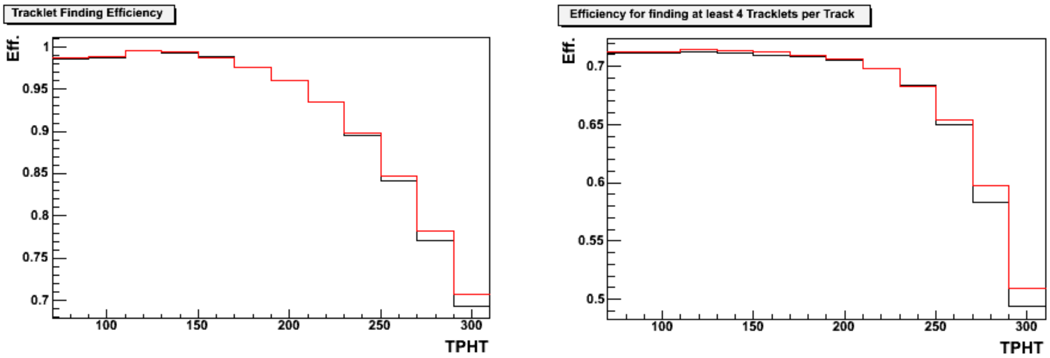

Figure 6.10: *Left:* Efficiency of assigning tracklets to MC track references. *Right:* Simplified Tracking Efficiency. (Red Curve: $B = 0\,\mathrm{T}$, Black: $B = 0.5\,\mathrm{T}$)

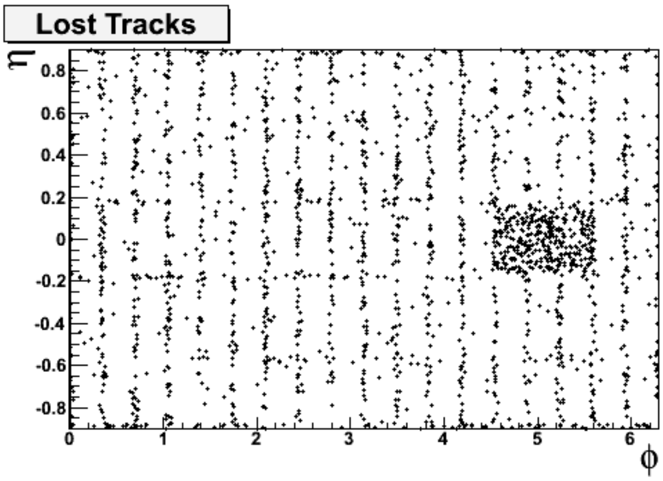

Figure 6.11: ϕ-η-distribution of lost tracks.

The last quantity to observe is the resolution. Therefore, a gaussian fit is applied on the Δy and the Δdy-distribution to obtain the resolutions σ_y and $\sigma_d y$ of the position and the deflection. The fitted resolutions can be found in figure 6.12.

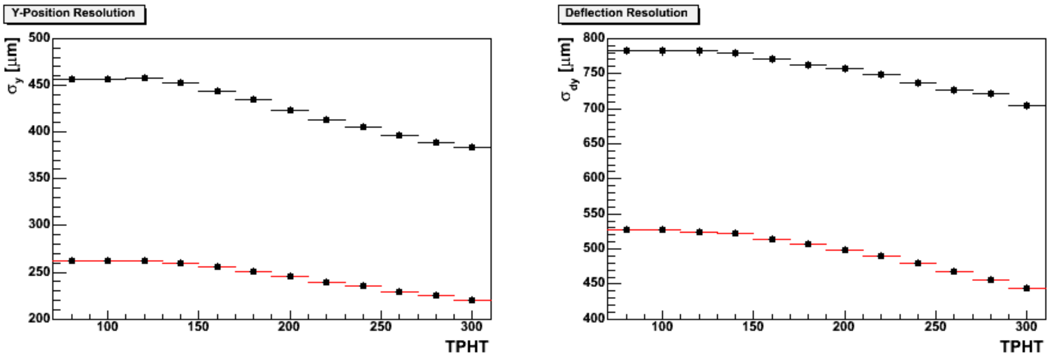

Figure 6.12: *Left:* Position Resolution *Right:* Deflection resolution. (Red Curve: $B = 0\,\mathrm{T}$, Black: $B = 0.5\,\mathrm{T}$)

It is quite obvious that the resolution is much better without magnetic field, for the position resolution about $200\,\mu$m and for the deflection resolution about $250\,\mu$m. The origin of this effect lies in the systematic shift due to the Lorentz deflection of the drifting electrons. More precisely, the effect can be explained with figure 6.6. If a particle travels through a chamber without a deflection dy_0 in y-direction, which is the mean of all particles if no magnetic field is applied, the resolution is the best and gets worse with larger $|dy - dy_0|$, as the influence of ion tails increases. In case of an applied field, the MCM measures no deflection if the particles angle of incident in y is just $-\Psi_L$. Actually, the dy_0 is shifted and therefore larger $|dy - dy_0|$ can occur which leads to a worse resolution for $B = 0.5\,\mathrm{T}$ than for $B = 0\,\mathrm{T}$.

6.2.3 Variation of the Tracklet Candidate Settings

The tracklet candidate settings determine the number of clusters needed to accept a tracklet and to perform the tracklet fit 4.4.2. The two thresholds $T_{C,L}$ and $T_{C,T}$ are stored within the TRAP registrs TPCL and TPCT. The choice of both parameters is not trivial, and therefore a set of simulations for different combinations of TPCL and TPCT has been made at TPHT $= 240$, since a case with fine resolution but no loss of too much efficiency wanted to be analysed. The range of TPCL has been chosen to be $[1, 6]$ and the one of TPCT was $[7, 16]$. For this, the number of simulated events has been reduced to 250 to save disk space and time. The same quantities as in section 6.2.2 have been studied.

In figure 6.13 the tracklet finding efficiency and the tracking efficiency is plotted for $B = 0\,\mathrm{T}$ abd $B = 0.5\,\mathrm{T}$. As in the TPHT efficiency analysis in figure 6.10, there is no large difference between the efficiencies for $B = 0\,\mathrm{T}$ and $B = 0.5\,\mathrm{T}$. Also, the tracking efficiencies seem to be quite stable for variations of TPCL as long as TPCT is also chosen small. Also there is a broad range of stable tracking efficiency at about 70 %, but for higher values

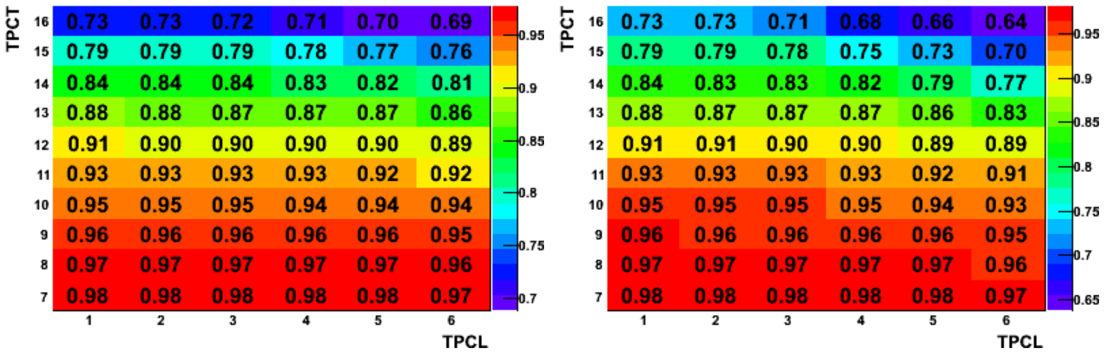

TPCT	1	2	3	4	5	6
16	0.73	0.73	0.72	0.71	0.70	0.69
15	0.79	0.79	0.79	0.78	0.77	0.76
14	0.84	0.84	0.84	0.83	0.82	0.81
13	0.88	0.88	0.87	0.87	0.87	0.86
12	0.91	0.90	0.90	0.90	0.90	0.89
11	0.93	0.93	0.93	0.93	0.92	0.92
10	0.95	0.95	0.95	0.94	0.94	0.94
9	0.96	0.96	0.96	0.96	0.96	0.95
8	0.97	0.97	0.97	0.97	0.97	0.96
7	0.98	0.98	0.98	0.98	0.98	0.97

(a) $B = 0\,\mathrm{T}$, Tracklet Efficiency

TPCT	1	2	3	4	5	6
16	0.73	0.73	0.71	0.68	0.66	0.64
15	0.79	0.79	0.78	0.75	0.73	0.70
14	0.84	0.83	0.83	0.82	0.79	0.77
13	0.88	0.87	0.87	0.87	0.86	0.83
12	0.91	0.91	0.90	0.90	0.89	0.89
11	0.93	0.93	0.93	0.93	0.92	0.91
10	0.95	0.95	0.95	0.95	0.94	0.93
9	0.96	0.96	0.96	0.96	0.96	0.95
8	0.97	0.97	0.97	0.97	0.97	0.96
7	0.98	0.98	0.98	0.98	0.98	0.97

(b) $B = 0.5\,\mathrm{T}$, Tracklet Efficiency

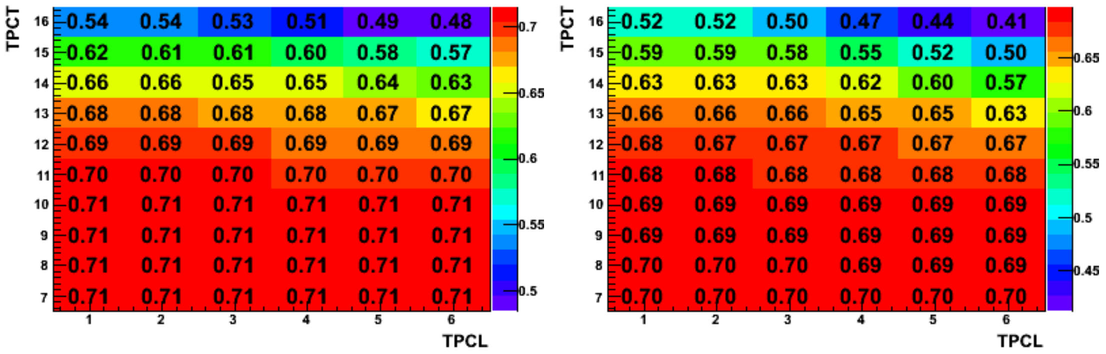

TPCT	1	2	3	4	5	6
16	0.54	0.54	0.53	0.51	0.49	0.48
15	0.62	0.61	0.61	0.60	0.58	0.57
14	0.66	0.66	0.65	0.65	0.64	0.63
13	0.68	0.68	0.68	0.68	0.67	0.67
12	0.69	0.69	0.69	0.69	0.69	0.69
11	0.70	0.70	0.70	0.70	0.70	0.70
10	0.71	0.71	0.71	0.71	0.71	0.71
9	0.71	0.71	0.71	0.71	0.71	0.71
8	0.71	0.71	0.71	0.71	0.71	0.71
7	0.71	0.71	0.71	0.71	0.71	0.71

(c) $B = 0\,\mathrm{T}$, Tracking Efficiency

TPCT	1	2	3	4	5	6
16	0.52	0.52	0.50	0.47	0.44	0.41
15	0.59	0.59	0.58	0.55	0.52	0.50
14	0.63	0.63	0.63	0.62	0.60	0.57
13	0.66	0.66	0.66	0.65	0.65	0.63
12	0.68	0.67	0.67	0.67	0.67	0.67
11	0.68	0.68	0.68	0.68	0.68	0.68
10	0.69	0.69	0.69	0.69	0.69	0.69
9	0.69	0.69	0.69	0.69	0.69	0.69
8	0.70	0.70	0.70	0.69	0.69	0.69
7	0.70	0.70	0.70	0.70	0.70	0.70

(d) $B = 0.5\,\mathrm{T}$, Tracking Efficiency

Figure 6.13: Tracklet and Tracking Efficiencies for $\mathrm{TPHT} = 240$ and variable TPCL and TPCT

than 13 in case of $B = 0\,\mathrm{T}$ or 12 in case of $B = 0.5\,\mathrm{T}$ for TPCT, the efficiency starts to fall. In figure 6.14 the fraction of noise tracklets is plotted. As expected, the noise is slightly higher for an applied magnetic field, but contrary to the efficiencies, the noise is falling almost linearly about 3-4 percentage points when increasing both TPCT and about 1-2 percentage points when increasing TPCL by 1. Therefore, noise can be significantly reduced by selecting higher TPCL and TPCT without a considerable loss of (especially tracking) efficiency

The last two parameters analysed for choosing TPCL and TPCT are again the resolutions of position and deflection. The effect of the both conditions on them are shown in figure 6.15. Again, the resolution difference between $B = 0\,\mathrm{T}$ and $B = 0.5\,\mathrm{T}$ observerd above is clearly visible. Also, the resolutions become worse linearly with increasing TPCT. For TPCL, the position resolution seems to have a minimum at $\mathrm{TPCL} = 4$, which is especially visible for $B = 0.5\,\mathrm{T}$, whereas the deflection resolution can be slightly improved by increasing TPCT. It is therefore suggestible to set the values of TPCL and TPCT values by exhausting the stable efficiency area, as this means a improvement of resolution and less noise at no significant loss of efficiency. Thus the initially set values of $\mathrm{TPCL} = 4$

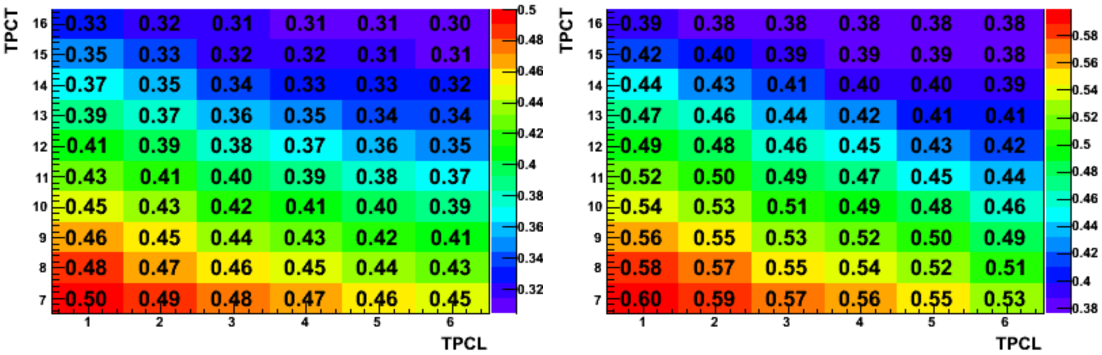
(a) $B = 0\,\mathrm{T}$ (b) $B = 0.5\,\mathrm{T}$

Figure 6.14: Noise fraction for $\mathrm{TPHT} = 240$ and variable TPCL and TPCT

and $\mathrm{TPCT} = 12$ seem to be a reasonable choice, but the values can be varied in a broad range according to specific needs.

6.3 Applying the Tail Cancellation Filter

The TC filter is the most complicated filter in the signal process; the cutting of the ADC-signal results in a improvement of the time resolution and thus also at least the resolution of the deflection and maybe also of the position, but also, as the ion tail is substracted, a loss of signal and therefore a worse signal-to-noise ratio. Therefore, to find the perfect balance, a good choice of the three configurable parameters λ_L, λ_S and α_L is necessary. So two sets of suggested parameters, presented in table 6.1 with the TRAP register values[2], will be anlysed, whereas the second set is more soft and therefore subtracts less signal from the input. The short decay length experiences the highest reduction to preserve more of the actual signal and focus on the longer ion tail.

Table 6.1: The two sets of parameters and their corresponding TRAP register values.

	λ_L	**FTLA**	λ_S	**FTLS**	α_L	**FTAL**
Set 1 [Gut02]	0.88925	285	0.35920	211	0.12017	246
Set 2 [Kle11]	0.84766	200	0.25000	0	0.09766	200

Adjustment of the default values

Due to the signal loss which occurs when applying the tail cancellation, some TRAP settings are changed to lower values, such that enough tracklets are found for the start.

---

[2] For a description of the conversions see [A+08b]

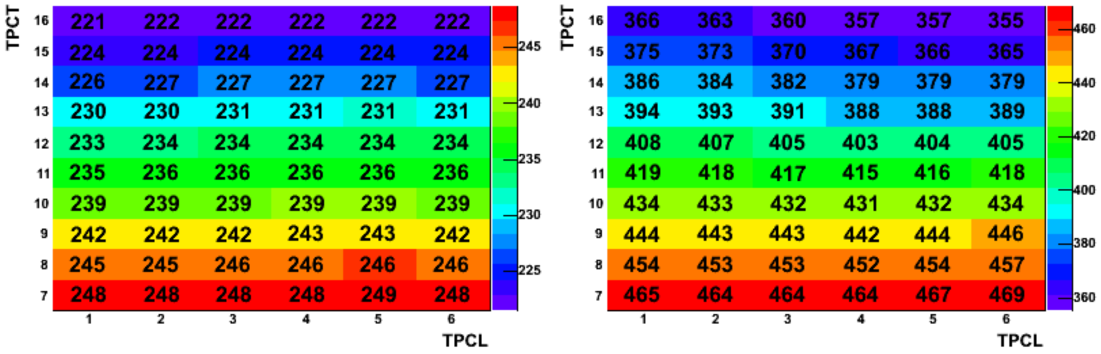

	1	2	3	4	5	6
16	221	222	222	222	222	222
15	224	224	224	224	224	224
14	226	227	227	227	227	227
13	230	230	231	231	231	231
12	233	234	234	234	234	234
11	235	236	236	236	236	236
10	239	239	239	239	239	239
9	242	242	242	243	243	242
8	245	245	246	246	246	246
7	248	248	248	248	249	248

(a) $B = 0\,\mathrm{T}$, $\sigma_y(\mu m)$

	1	2	3	4	5	6
16	366	363	360	357	357	355
15	375	373	370	367	366	365
14	386	384	382	379	379	379
13	394	393	391	388	388	389
12	408	407	405	403	404	405
11	419	418	417	415	416	418
10	434	433	432	431	432	434
9	444	443	443	442	444	446
8	454	453	453	452	454	457
7	465	464	464	464	467	469

(b) $B = 0.5\,\mathrm{T}$, $\sigma_y(\mu m)$

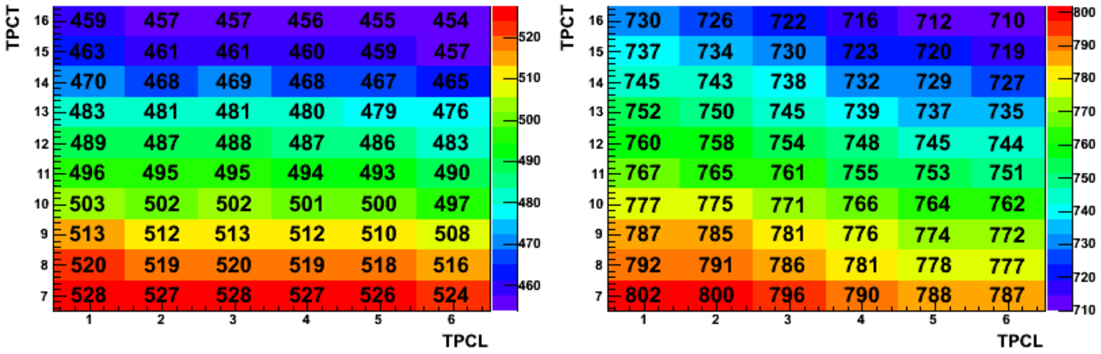

	1	2	3	4	5	6
16	459	457	457	456	455	454
15	463	461	461	460	459	457
14	470	468	469	468	467	465
13	483	481	481	480	479	476
12	489	487	488	487	486	483
11	496	495	495	494	493	490
10	503	502	502	501	500	497
9	513	512	513	512	510	508
8	520	519	520	519	518	516
7	528	527	528	527	526	524

(c) $B = 0\,\mathrm{T}$, $\sigma_{dy}(\mu m)$

	1	2	3	4	5	6
16	730	726	722	716	712	710
15	737	734	730	723	720	719
14	745	743	738	732	729	727
13	752	750	745	739	737	735
12	760	758	754	748	745	744
11	767	765	761	755	753	751
10	777	775	771	766	764	762
9	787	785	781	776	774	772
8	792	791	786	781	778	777
7	802	800	796	790	788	787

(d) $B = 0.5\,\mathrm{T}$, $\sigma_{dy}(\mu m)$

Figure 6.15: Position and Deflection resolution for $\mathrm{TPHT} = 240$ and variable TPCL and TPCT

The scaled down values are based on preceding analysises [Wal10]. The changed default values are shown in table 6.2:

Table 6.2: Changed default settings for analysis with the TC filter.

Register	Old setting	New setting set 1	New setting set 2
TPHT	240	150	150
TPFP	40	20	30
TPCL	4	2	2
TPCT	12	10	10

6.3.1 Parameter Set 1

At first the parameter set 1 will be analysed for a comparision to the analysis without the TC filter and then later compared to set 2. Therefore, the same methods as in section 6.2 are applied:

Adjustment of the drift time

As the tail cancellation's intention is to remove the time response effects on the ADCs, the correct drift time has to be adjustet again. With the same method applied as in section 6.2.1 the new calculated intersection point is $t_{drift,1} = 19.762$ timebins. As expected, the calculated drift time is much closer to the value of 20 timebins than without an applied tail cancellation. However, it is slightly smaller which could be a hint of too much signal reduction.

Variation of TPHT

For the variation of the cluster threshold the window has been shrinked from TPHT = 80 to TPHT = 240, as much higher values are not expected to provide good efficiencies due to the signal reduction. In figure 6.16 the number of found tracklets and the noise fraction for set 1 are plotted. Again more tracklets, which mainly contribute to the noise fraction, are found if the magnetic field is switched on. The noise clearly has a minum at TPHT = 120 and then raises rapidly. In comparison to a switched off TC, the noise fraction falls and raises stronger with changing TPHT with an applied TC filter, but lies within the same range. The faster decrease is also observable for the efficiencies shown in figure 6.17. The tracklet finding efficiency falls alsmost linearly to zero and even faster does the tracking efficiency. By looking at the dependency of resolutions from TPHT in figure 6.18, one can also observe the strong dependency on TPHT. Therefore, the choice of a reasonable value for TPHT proves more difficult than without a TC filter, as particulary the position resolution gets worse faster than without TC. But, the difference between the deflection resolution for $B = 0\,\mathrm{T}$ and $B = 0.5\,\mathrm{T}$ was reduced from ca. $250\,\mu\mathrm{m}$ to approximately $150\,\mu\mathrm{m}$, resulting in achievable resolutions up to $150\,\mu\mathrm{m}$ better than without TC at only small efficiency differences (see for example $TPHT = 120$ with TC and $TPHT = 240$

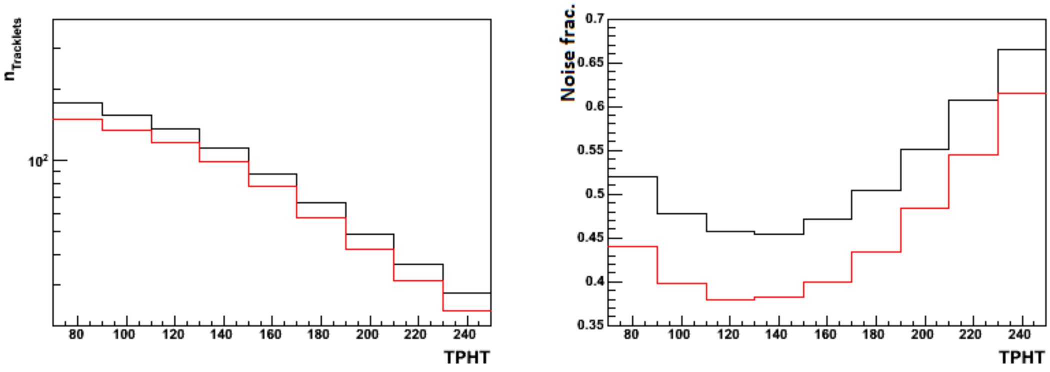

Figure 6.16: Set 1: Average number of tracklets per event (left) with noise fraction (right) vs. TPHT. (Red Curve: $B = 0\,\mathrm{T}$, Black: $B = 0.5\,\mathrm{T}$)

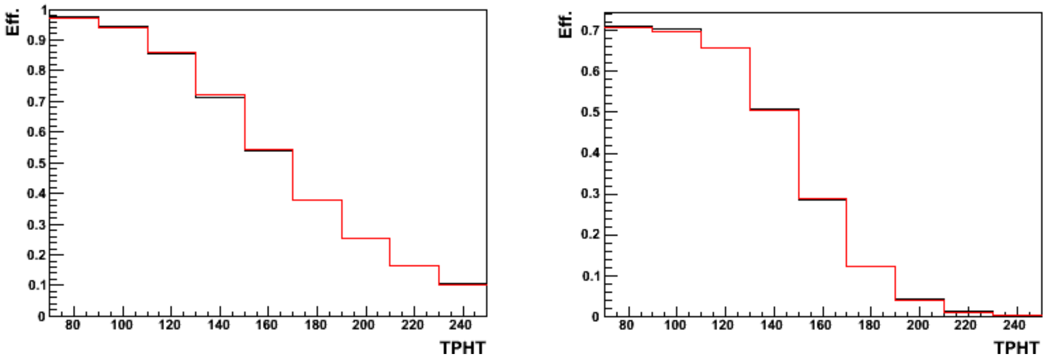

Figure 6.17: Set 1: Efficiencies vs. TPHT.*Left:* Tracklet efficiency. *Right:* Tracking efficiency. (Red Curve: $B = 0\,\mathrm{T}$, Black: $B = 0.5\,\mathrm{T}$)

without TC). Also the position resolution can be slightly improved, especially for the case of an applied magnetic field.

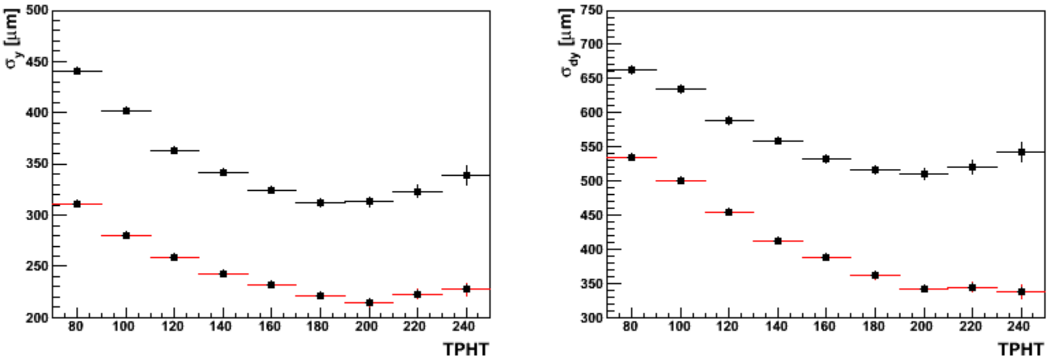

Figure 6.18: Set 1: Resolution vs. TPHT. *Left:* Position resolution. *Right:* Deflection resolution. (Red Curve: $B = 0\,\mathrm{T}$, Black: $B = 0.5\,\mathrm{T}$)

Variation of TPCL and TPCT

Like the TPHT also the window of TPCT has been narrowed from 6 to 14 while TPCL is still reaching from 1 to 6. As cluster threshold TPHT = 120 has been chosen. First, a look is taken on the efficiencies in figure 6.19 for both cases $B = 0.5\,\mathrm{T}$ and $B = 0\,\mathrm{T}$.

First, a look is taken at the efficiencies in figure 6.19 for the both cases $B = 0.5\,\mathrm{T}$ and $B = 0\,\mathrm{T}$. The situation is in the fashion of the case without a TC filter. The tracking efficiency is stable at around 70%, this time one can classify TPCL = 3 and TPCT = 8 as the point from where the increasing of one value results in a noticable efficiency loss. Again at this point, the efficiency for finding a tracklet falls below 90%. An interesting effect, which is also observable without a TC filter (figure 6.13) but comes into view slightly better with the TC switched on, is that, for $B = 0\,\mathrm{T}$, the tracking efficiency provides a marginally

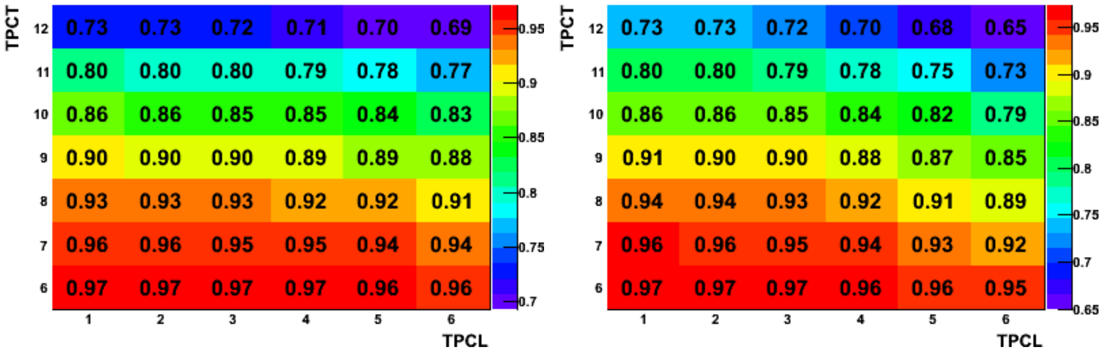

(a) $B = 0\,\mathrm{T}$, Tracklet Efficiency (b) $B = 0.5\,\mathrm{T}$, Tracklet Efficiency

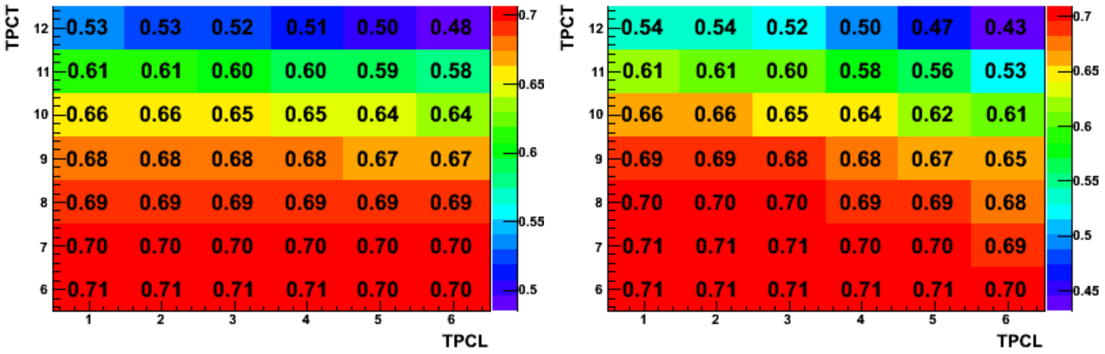

(c) $B = 0\,\mathrm{T}$, Tracking Efficiency (d) $B = 0.5\,\mathrm{T}$, Tracking Efficiency

Figure 6.19: Set 1: Tracklet and Tracking Efficiencies for variable TPCL and TPCT

faster decrease with TPCL at an approximately same tracklet finding efficiency in both cases, but on the other hand is (including the tracklet finding efficiency slightly more stable for variations of TPCT. The better stability for varying TPCT can be explained by the systematically shifted deflection of tracklets for $B = 0.5\,\mathrm{T}$. The faster decreasing tracking efficiency for $B = 0\,\mathrm{T}$ can be explained if one considers, that the curvature induced by the solenoid field, is able to curve tracks from the IP out of and into dead zones. Therefore particles which travel through dead zones can still be tracked in other modules, while a particle that enters a dead zone is lost in case of no magnetic field.

Finally, the broad area of assignable values for adequate stable efficencies offers the opportunity to look for well noise reduction and better resolutions in that range once more. An investigation of the tracklet noise fraction in figure 6.20 shows again an approximately linear decrease of noise with no noticeable change compared to a switched off TC filter.

The resolutions, plotted in figure 6.21, show a stronger stability for changes of the TPCL value thant without a TC filter. Especially for the magnetic field, the deflection resolution gets only slightly worse when reducing TPCL, which allows a choice of small TPCL values. The resolution dependency on TPCT shows no noticeable difference to the case without a magnetic field.

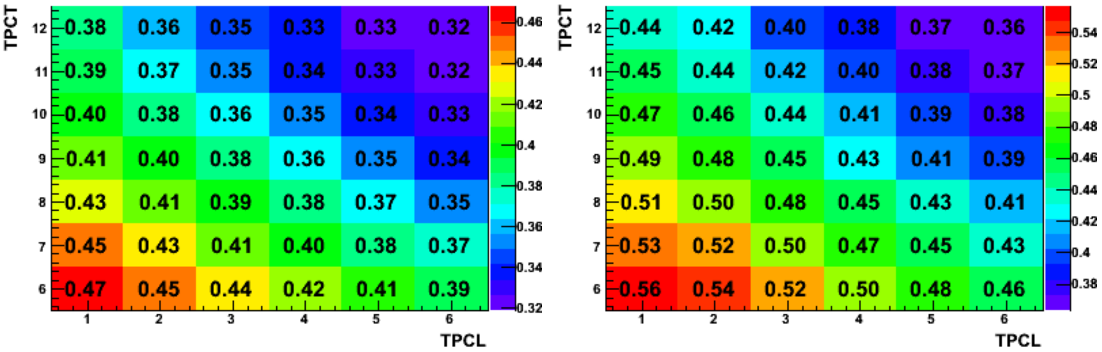

(a) $B = 0\,\mathrm{T}$ (b) $B = 0.5\,\mathrm{T}$

Figure 6.20: Set 1: Noise fraction for variable and variable TPCL and TPCT

6.3.2 Parameter Set 2

In the following, a second set of TC parameters (as listed in table 6.1) will be applied. As the differences between switched off and switched on TC filter have just been discussed, this section will focus on the comparision of the two parameter sets among themselves.

Adjustment of the drift time

The drift time calculated for set 2 is $t_{drift,2} = 21.724$ timebins, which is a larger difference from $t_{drift} = 20$ timebins than for set 1. As the second set subtracts less signal that was to be expected.

Variation of TPHT

The same TPHT range as before has been chosen for the analysis, to provide an easy overview of the effects and differences the new sets causes. By studying the plots in figure 6.22 and comparing them to figure 6.16 and 6.17, the difference in signal reduction becomes quite clear as the plots seem just to be shifted to the right ($\Delta\mathrm{TPHT} \approx 40$). Apart from the shift, the behaviour of the curves shows no noticeable difference from each other. This changes for the resolutions which are visualised in figure 6.23. It is obvious that for the second set of parameters the resolutions are not related to TPHT that strong like for set 1. At comparable efficiencies, which is approximatley the case for $\mathrm{TPHT}_{\mathrm{Set1}} = \mathrm{TPHT}_{\mathrm{Set2}} - 40$, the deflection resolution is slightly better for set 2 until its TPHT reaches 180 if one can abandon an magnetic field. However, the deflection resolution is overall worse about 50 μm to 100 μm, but still approximately 100 μm better than without tail cancellation. The same effect is visible for the position resolution.

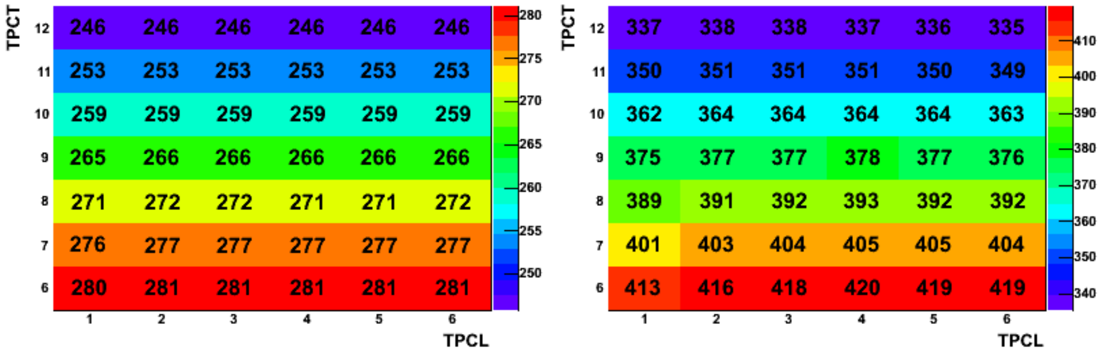

TPCT \ TPCL	1	2	3	4	5	6
12	246	246	246	246	246	246
11	253	253	253	253	253	253
10	259	259	259	259	259	259
9	265	266	266	266	266	266
8	271	272	272	271	271	272
7	276	277	277	277	277	277
6	280	281	281	281	281	281

(a) $B = 0\,\mathrm{T}$, $\sigma_y(\mu m)$

TPCT \ TPCL	1	2	3	4	5	6
12	337	338	338	337	336	335
11	350	351	351	351	350	349
10	362	364	364	364	364	363
9	375	377	377	378	377	376
8	389	391	392	393	392	392
7	401	403	404	405	405	404
6	413	416	418	420	419	419

(b) $B = 0.5\,\mathrm{T}$, $\sigma_y(\mu m)$

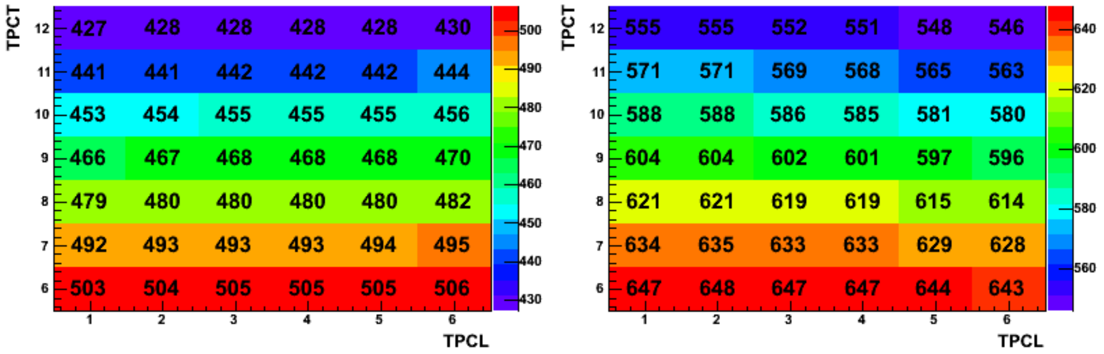

TPCT \ TPCL	1	2	3	4	5	6
12	427	428	428	428	428	430
11	441	441	442	442	442	444
10	453	454	455	455	455	456
9	466	467	468	468	468	470
8	479	480	480	480	480	482
7	492	493	493	493	494	495
6	503	504	505	505	505	506

(c) $B = 0\,\mathrm{T}$, $\sigma_{dy}(\mu m)$

TPCT \ TPCL	1	2	3	4	5	6
12	555	555	552	551	548	546
11	571	571	569	568	565	563
10	588	588	586	585	581	580
9	604	604	602	601	597	596
8	621	621	619	619	615	614
7	634	635	633	633	629	628
6	647	648	647	647	644	643

(d) $B = 0.5\,\mathrm{T}$, $\sigma_{dy}(\mu m)$

Figure 6.21: Set 1: Position and Deflection resolution for variable TPCL and TPCT

Variation of TPCL and TPCT

For the variation of the cluster candidate settings TPCL and TPCT, the range of parameter set 1 has been adopted as it stands. As cluster threshold TPHT = 160 was chosen, as the efficiencies there are comparable to the TPCL and TPCT analysis of set 1. At first, again the efficiencies and noise are compared. The plots have been taken together in figure 6.24, as there can be observed no remarkable trend differences for the two sets of TC parameters.

The resolutions are shown seperately in figure 6.25. For the position resolution, the behaviour is almost the same to parameter set 1, while the deflection resolution shows a stronger dependency on TPCL than TPCT.

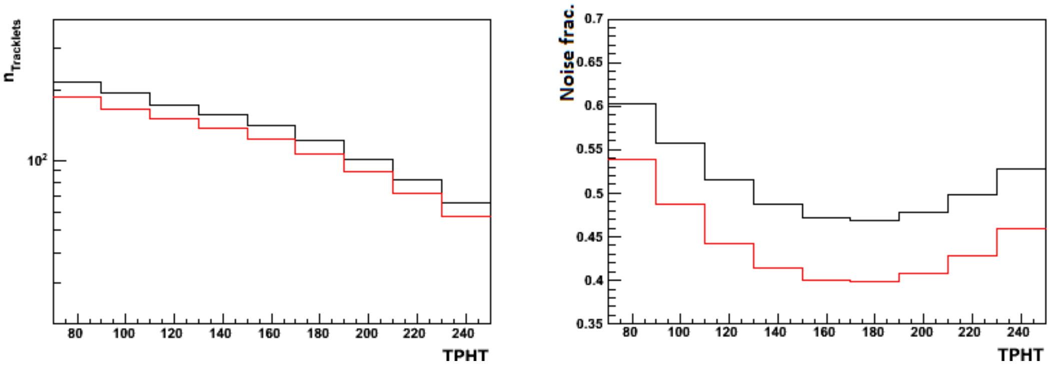

(a) Average $n_{tracklets}$/ev (b) Noise Fraction

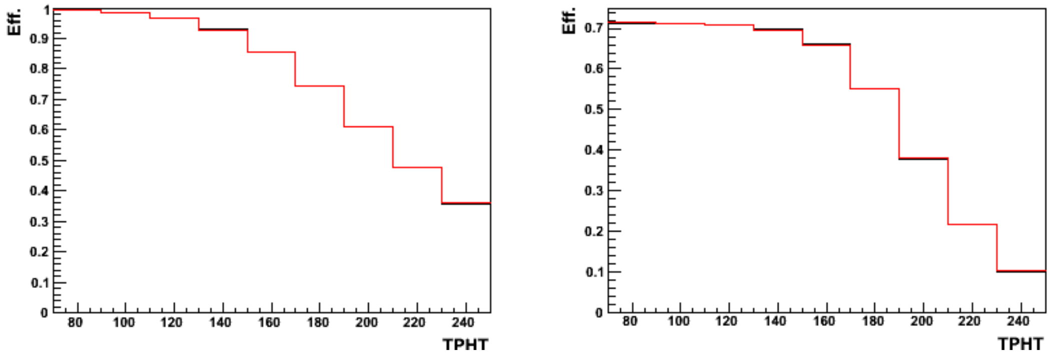

(c) Tracklet finding efficiency (d) Tracking efficiency

Figure 6.22: Set 2: TPHT dependency plots. (Red Curve: $B = 0\,\mathrm{T}$, Black: $B = 0.5\,\mathrm{T}$)

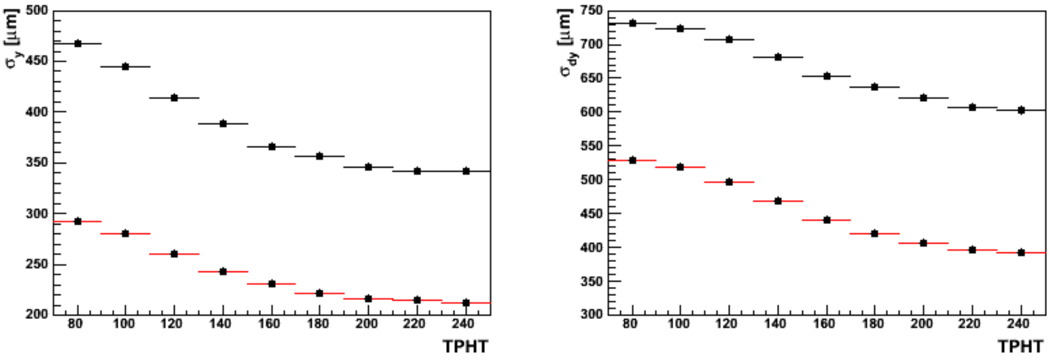

Figure 6.23: Set 2: Resolution vs. TPHT. *Left:* Position resolution. *Right:* Deflection resolution. (Red Curve: $B = 0\,\mathrm{T}$, Black: $B = 0.5\,\mathrm{T}$)

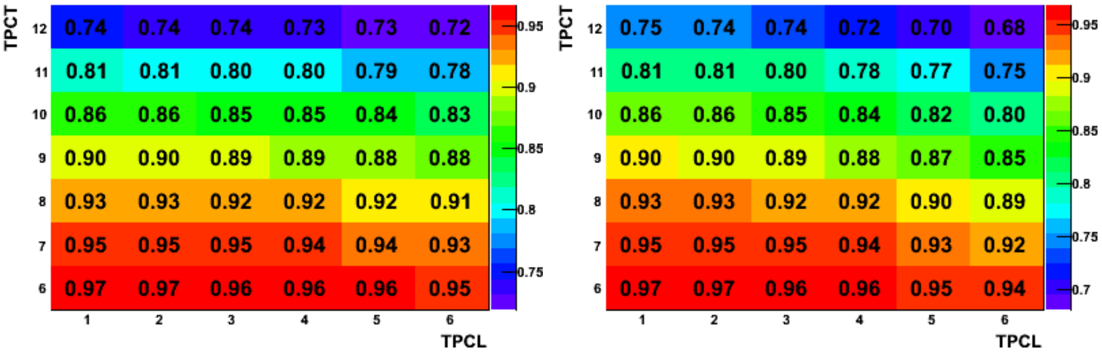

TPCT / TPCL	1	2	3	4	5	6
12	0.74	0.74	0.74	0.73	0.73	0.72
11	0.81	0.81	0.80	0.80	0.79	0.78
10	0.86	0.86	0.85	0.85	0.84	0.83
9	0.90	0.90	0.89	0.89	0.88	0.88
8	0.93	0.93	0.92	0.92	0.92	0.91
7	0.95	0.95	0.95	0.94	0.94	0.93
6	0.97	0.97	0.96	0.96	0.96	0.95

(a) $B = 0\,\mathrm{T}$, Tracklet Efficiency

TPCT / TPCL	1	2	3	4	5	6
12	0.75	0.74	0.74	0.72	0.70	0.68
11	0.81	0.81	0.80	0.78	0.77	0.75
10	0.86	0.86	0.85	0.84	0.82	0.80
9	0.90	0.90	0.89	0.88	0.87	0.85
8	0.93	0.93	0.92	0.92	0.90	0.89
7	0.95	0.95	0.95	0.94	0.93	0.92
6	0.97	0.97	0.96	0.96	0.95	0.94

(b) $B = 0.5\,\mathrm{T}$, Tracklet Efficiency

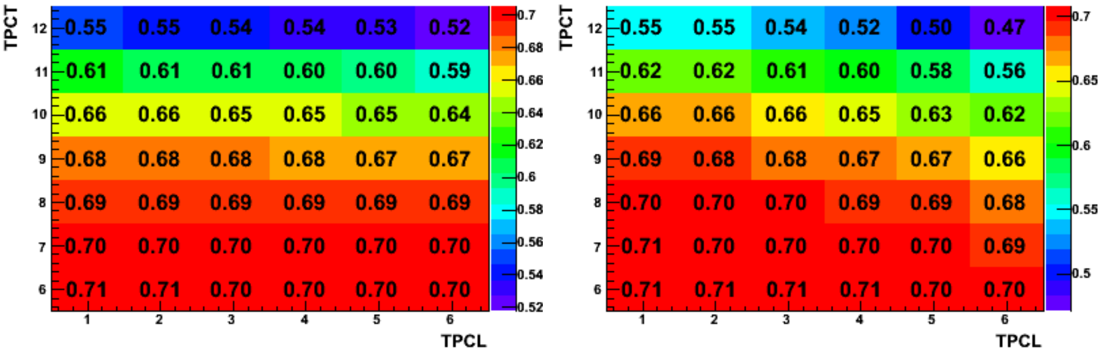

TPCT / TPCL	1	2	3	4	5	6
12	0.55	0.55	0.54	0.54	0.53	0.52
11	0.61	0.61	0.61	0.60	0.60	0.59
10	0.66	0.66	0.65	0.65	0.65	0.64
9	0.68	0.68	0.68	0.68	0.67	0.67
8	0.69	0.69	0.69	0.69	0.69	0.69
7	0.70	0.70	0.70	0.70	0.70	0.70
6	0.71	0.71	0.70	0.70	0.70	0.70

(c) $B = 0\,\mathrm{T}$, Tracking Efficiency

TPCT / TPCL	1	2	3	4	5	6
12	0.55	0.55	0.54	0.52	0.50	0.47
11	0.62	0.62	0.61	0.60	0.58	0.56
10	0.66	0.66	0.66	0.65	0.63	0.62
9	0.69	0.68	0.68	0.67	0.67	0.66
8	0.70	0.70	0.70	0.69	0.69	0.68
7	0.71	0.70	0.70	0.70	0.70	0.69
6	0.71	0.71	0.71	0.71	0.70	0.70

(d) $B = 0.5\,\mathrm{T}$, Tracking Efficiency

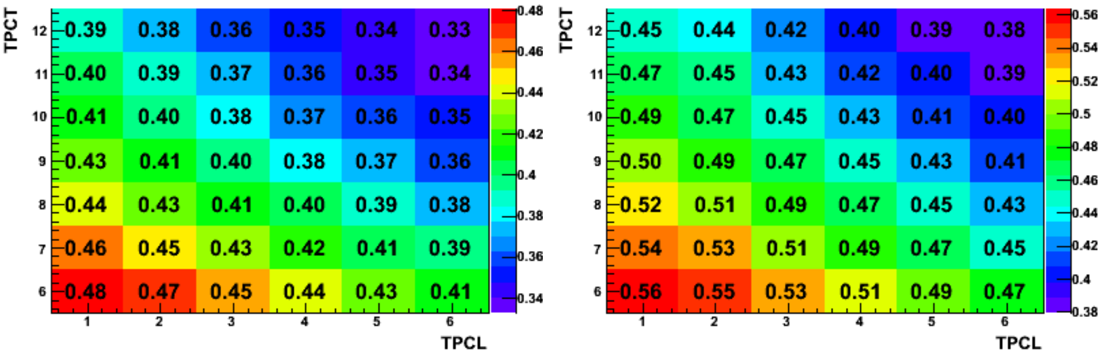

TPCT / TPCL	1	2	3	4	5	6
12	0.39	0.38	0.36	0.35	0.34	0.33
11	0.40	0.39	0.37	0.36	0.35	0.34
10	0.41	0.40	0.38	0.37	0.36	0.35
9	0.43	0.41	0.40	0.38	0.37	0.36
8	0.44	0.43	0.41	0.40	0.39	0.38
7	0.46	0.45	0.43	0.42	0.41	0.39
6	0.48	0.47	0.45	0.44	0.43	0.41

(e) $B = 0\,\mathrm{T}$, Noise Fraction

TPCT / TPCL	1	2	3	4	5	6
12	0.45	0.44	0.42	0.40	0.39	0.38
11	0.47	0.45	0.43	0.42	0.40	0.39
10	0.49	0.47	0.45	0.43	0.41	0.40
9	0.50	0.49	0.47	0.45	0.43	0.41
8	0.52	0.51	0.49	0.47	0.45	0.43
7	0.54	0.53	0.51	0.49	0.47	0.45
6	0.56	0.55	0.53	0.51	0.49	0.47

(f) $B = 0.5\,\mathrm{T}$, Noise Fraction

Figure 6.24: Set 2: Tracklet and Tracking Efficiencies for variable TPCL and TPCT

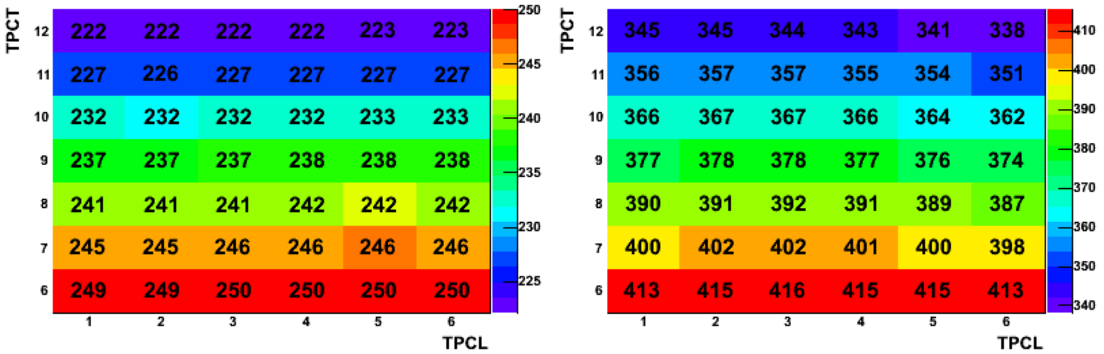

TPCT \ TPCL	1	2	3	4	5	6
12	222	222	222	222	223	223
11	227	226	227	227	227	227
10	232	232	232	232	233	233
9	237	237	237	238	238	238
8	241	241	241	242	242	242
7	245	245	246	246	246	246
6	249	249	250	250	250	250

(a) $B = 0\,\mathrm{T}$, $\sigma_y(\mu m)$

TPCT \ TPCL	1	2	3	4	5	6
12	345	345	344	343	341	338
11	356	357	357	355	354	351
10	366	367	367	366	364	362
9	377	378	378	377	376	374
8	390	391	392	391	389	387
7	400	402	402	401	400	398
6	413	415	416	415	415	413

(b) $B = 0.5\,\mathrm{T}$, $\sigma_y(\mu m)$

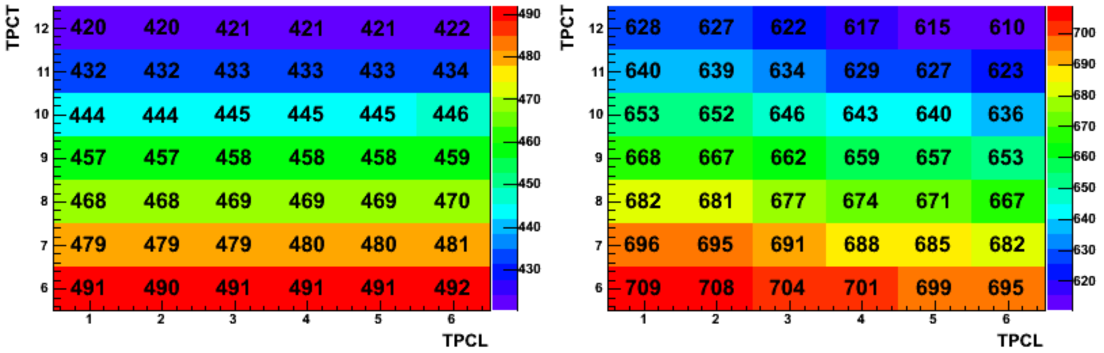

TPCT \ TPCL	1	2	3	4	5	6
12	420	420	421	421	421	422
11	432	432	433	433	433	434
10	444	444	445	445	445	446
9	457	457	458	458	458	459
8	468	468	469	469	469	470
7	479	479	479	480	480	481
6	491	490	491	491	491	492

(c) $B = 0\,\mathrm{T}$, $\sigma_{dy}(\mu m)$

TPCT \ TPCL	1	2	3	4	5	6
12	628	627	622	617	615	610
11	640	639	634	629	627	623
10	653	652	646	643	640	636
9	668	667	662	659	657	653
8	682	681	677	674	671	667
7	696	695	691	688	685	682
6	709	708	704	701	699	695

(d) $B = 0.5\,\mathrm{T}$, $\sigma_{dy}(\mu m)$

Figure 6.25: Set 2: Position and Deflection resolution for variable TPCL and TPCT

7 Summary and Discussion

Finally, to come to a conclusion, the analysis and observations made in this thesis shall be summarised. At first, an idealistic study of a jet trigger realisable with the TRD has been presented on the basis of Monte-Carlo data. The efficiency for triggering on jet events and the rejection of minimum bias events were evaluated. Several conditions on the number of charged particles per TRD stack $n_{min} = \{2, 3, 4\}$ and their transverse momentum threshold $p_{T,min} = \{2, 3, 4\}\,\mathrm{GeV}$ have been applied and the dependency of efficiency and rejection was analysed. Small values improved efficiency, especially for low energetic jets, but also strongly worsen the rejection. For the applied conditions, the rejection varied from approximately 131 ± 11 to for the loosest ($n_{min} = 2$, $p_{T,min} = 2\,\mathrm{GeV}$) to 50800 ± 200 for the most suppressive ($n_{min} = 4, p_{T,min} = 4\,\mathrm{GeV}$) with a nearly exponential dependency observed. A moderate condition with $n_{min} = 2$, $p_{T,min} = 2\,\mathrm{GeV}$ provides a rejection of 3920 ± 60. Assuming 100 kHz as a typical working rate of the TPC [Kle11], these rejections seem to be quite reasonable as they are at least partially able to provide a trigger rate of few Hz. Considering the efficiency for jet triggering as a function of the leading jet p_T, a raise of the thresholds stretched the efficiency curve to higher leading jet p_Ts. For $n_{min} = 2$ and $p_{T,min} = 2\,\mathrm{GeV}$, the efficiency already reaches 80 % for a leading jet transverse momentum of $p_t = 50\,\mathrm{GeV}$, while for the highest thresholds (see above) it is reached not before a leading jet p_t of $250\,\mathrm{GeV}$. For the moderate condition 80 % efficiency is achieved at $p_T = 120\,\mathrm{GeV}$ for the leading jet. Considering the achievable trigger rates and the quite reasonable efficiencies, a jet trigger can be realised, but has to undergo more studies including GTU tracking and could be tested on already recorded *pp* minimum bias raw data.

The most important requirement for an operative jet trigger based on high p_T particles is a fast and precise determination of the track's transverse momentum p_T, which is done by the GTU. As the GTU uses the tracklets calculated in each MCM for the transverse momentum determination, an accurate calculation of the tracklets is very importants. To analyse the performance and quailty of the tracklet processing, the position and deflection resolutions of those tracklets have been studied besides the efficiency and noise fraction of the tracklet determination. Also the efficiency of an idealistic tracking, assuming that each particle with a tracklet in at least four TRD layers is tracked certainly, was studied. As the TRAP chips in the MCM's allow a broad range of settings, including corrections, the digital filters and the conditions for tracklet processing, the settings relevant for the

abovementioned quantites have been varied to study their effects on them. First of all, the corrections for the pad tilting and the Lorentz deflection had been applied successfully. The position determination of the charge deposition could be raised above the technological granularity by the Pad-Response-Function and the effect of ion tails on the effective drift time could be eliminated.
Beginning with no tail cancellation and a switched off solenoid field, position resolutions up to $\sigma_y = 235\,\mu m$ and deflection resolutions up to $\sigma_{dy} = 490\,mu$ at 70 % tracking efficiency (dead zones were included) and over 90 % tracklet efficiency with a noise fraction of about 40 % were achievable. All quantities showed a dependency on the cluster threshold TPHT especially for higher values, so that higher settings of TPHT reduce the noise fraction and improve resolution, but also lead to a decrease of efficiency. Also a dependency on TPCL and TPCT could be observerd, with higher values generally improving resolution and noise but also decrease the efficiencies. The dependence on TPCT was found to be stronger than the one on TPCL, were the quantities are more stable for changes.
With the application of the tail cancellation filter, which was evaluated with two different sets of parameters, the deflection resolution could be slightly improved up to $\sigma_{dy} = 450 - 460\,\mu$m for both sets while the position resolution could be retained for set 2 but became about $20\,\mu$m worse for set 1, which was configured to substract more signal than set 2, at comparable efficiencies and noise fraction. Furthermore a strong dependency on TPHT and TPCT for set 2 and an even stronger one for set 1 could be observed compared to no applied tail cancellation accounted for by the worse signal-to-noise ratio during the tracklet calculation due to the subtraction of signal by the filter. For variations of TPCL the resolutions showed almost no reaction. The advantages of the tail cancellation first can be really observed with an applied magnetic field. If the field of $B = 0.5\,,$T is applied without the tail cancellation filter, the position and deflection resolution become worse to $\sigma_y = 400\,\mu m$ and $\sigma_{dy} = 750\,mu$ at comparable efficiencies. Also the noise fraction raises about 7 percentage points to about 47 %.
In the case of an active tail cancellation filter, this deterioration of the resolutions can be weakened. For parameter set 1, the resolutions only worsen to $\sigma_y = 370\,\mu m$ and $\sigma_{dy} = 590\,\mu m$ at comparable efficiencies and for parameter set 2 to $\sigma_y = 370\,\mu m$ and $\sigma_{dy} = 660\,\mu m$.

As the magnetic field is absolutely necessary for a reasonable operation of ALICE and best possible resolutions at high efficiency are desirable for a high-p_T jet trigger, the application of the tail cancellation with parameter set 1 could be suggested. However, the problem of the first parameter set is the large signal reduction which can be seen at the low threshold TPHT = 120 which needed to be chosen to fulfill 70 % tracking efficiency in comparision to set 2 (TPHT = 160), as the signal strength is very important to the TRD PID calculation and therefore to other triggers like an e^+e^--trigger. Consequently, studies of PID and tracking performance must be brought in line as long as one is not willing to neglect certain triggers of the TRD.

One also has to consider that the analysis has been performed in an easy environment with 10 proton and 10 anti-protons fired into the TRD. Thus, a further analysis should be performed on *pp* and also *PbPb* events, preferably with high multiplicities, to observe the effect of a broader range and greater number of particles. Also it could be tested on raw data if an adjustment of the settings in the offline reconstruction leads to a better resolution for the reconstructed tracklets than the one gained online and stored in the tracklet word.

Bibliography

[A$^+$08a] K. Aamodt et al. The ALICE experiment at the CERN LHC. *JINST*, 3:S08002, 2008.

[A$^+$08b] Venelin Angelov et al. ALICE TRAP User Manual. Technical report, 2008.

[A$^+$10] K. Aamodt et al. Charged-Particle Multiplicity Density at Midrapidity in Central Pb-Pb Collisions at $\sqrt{s_{NN}} = 2.76\,\mathrm{TeV}$. *Phys. Rev. Lett.*, 105(25):252301, Dec 2010.

[ALI07] ALICE. Der Zugang zum Quark-Gluon-Plasma, 2007. URL: `http://www-alice.gsi.de/fsp201/intro/Alice_brochure_P23_v023_lr.pdf`.

[ALI10] ALICE. Official Website of the ALICE Collaboration, 4 2010. URL: `http://aliceinfo.cern.ch/`.

[ALI11] ALICE. AliROOT Documentation, 2011. URL: `http://aliceinfo.cern.ch/Offline/AliRoot/Manual.html`.

[B$^+$79] D. P. Barber et al. Discovery of Three Jet Events and a Test of Quantum Chromodynamic at PETRA Energies. *Phys. Rev. Lett.*, 43:830, 1979.

[Ber06] Christoph Berger. *Elementarteilchenphysik - Von den Grundlagen zu den modernen Experimenten.* Springer, 2006. DOI: 10.1007/3-540-33594-3.

[Boc98] R.-K. Bock. Transition Radiation, 9 1998. http://rkb.home.cern.ch/rkb/PH14pp/node194.html.

[CER06] CERN. CERN Confident of LHC start-up in 2007, 12 2006. URL: `http://public.web.cern.ch/press/pressreleases/releases2006/PR20.06E.html`.

[CER11] CERN. Official CERN Website, 2011. URL: `http://public.web.cern.ch`.

[Col01] The ALICE Collaboration. ALICE Technical Design Report of the Transition Radiation Detector. Technical Report 021, CERN, 2001.

[Col03] The ALEPH Collaboration. Measurements of the strong coupling constant and the QCD colour factors using four-jet observables from hadronic Z decays. *The European Physical Journal C - Particles and Fields*, 27:1–17, 2003. 10.1140/epjc/s2002-01114-2.

[dC08] Jan de Cuveland. Entwicklung der globalen Spurrekonstruktionseinheit für den ALICE-Übergangsstrahlungsdetektor am LHC (CERN). Diploma thesis, University of Heidelberg, 2008.

[EHH$^+$07] S. D. Ellis, J. Huston, K. Hatakeyama, P. Loch, and M. Tönnesmann. Jets in Hadron-Hadron Collisions. *test*, 2007. arXiv:0712.2447 [hep-ph].

[Fla01] Uwe Flagmeyer. *Multijet-Produktion in der e^+e^--Annihilation von $\sqrt{s} =$ 98 GeV bis 207 Gev*. PhD thesis, University of Wuppertal, 2001.

[Gro08] CERN Communication Group. LHC - The Guide, 1 2008. URL: `http://cdsweb.cern.ch/record/1092437/files/CERN-Brochure-2008-001-Eng.pdf`.

[Gut02] Marcus Gutfleisch. Digitales Frontend und Preprozessor im TRAP1-Chip des TRD Triggers fuer das ALICE Experiment am LHC (CERN). Diploma thesis, University of Heidelberg, 2002.

[Kle08] Jochen Klein. Commissioning of and Preperations for Physics with the Transition Radiation Detector in A Large Ion Collider Experiment at CERN. Diploma thesis, University of Heidelberg, 2008.

[Kle11] Jochen Klein. Private Communication, 2011.

[MIM04] MIMD Rechnerarchitekturen. Lecture, 2003/2004. URL: `http://ra.ziti.uni-heidelberg.de/pages/lectures/hws08/ra2/script_pdf/basics_mimd.pdf`.

[Sch08] R. Schicker. The ALICE detector and trigger strategy for diffractive and electromagnetic processes. *Nucl. Phys. Proc. Suppl.*, 179-180:196–201, 2008.

[Wal10] Matthias Walter. Performance of Online Tracklet Reconstruction with the ALICE TRD. Diploma thesis, University of Muenster, 2010.

[Wul09] Elke Svenja Wulff. Position Resolution and Zero Suppression of the ALICE TRD. Diploma thesis, University of Muenster, 2009.

Acknowledgements

First of all, I want to thank Prof. Dr. Johanna Stachel for providing the great opportunity to perform this bachelor thesis and taking part in the group meetings.
I would particulary like to thank Jochen Klein for his great effort on supporting me in my studies, his always very qualified advices and the detailed review of my thesis.
Furthermore I am very grateful for Oliver Busch for his eager support at my first steps with AliROOT and the trigger studies. Special thanks also go to Martin Gabel for the computer support and Benjamin Heß for his advice. Last but not least, I want to give my thanks to the additional members of the workgroup and my friends and family for the support during the three months of my studies.

Erklärung

Ich versichere, dass ich diese Arbeit selbstständig verfasst und keine anderen als die angegebenen Quellen und Hilfsmittel benutzt habe.

Heidelberg, den 14. April 2011

....
Niklas Wahl